AD_____

Award Number: W81XWH-04-1-0240

TITLE: High Resolution Anatomic and Elastographic Transrectal Ultrasound for Improved Diagnosis of Prostate Cancer

PRINCIPAL INVESTIGATOR: John A. Hossack, Ph.D.

CONTRACTING ORGANIZATION: University of Virginia
Charlottesville, VA 22908-0759

REPORT DATE: August 2008

TYPE OF REPORT: Final

PREPARED FOR: U.S. Army Medical Research and Materiel Command
Fort Detrick, Maryland 21702-5012

REPORT DOCUMENTATION PAGE

Form Approved
OMB No. 074-0188

Public reporting burden for this collection of information is estimated to average 1 hour per response, including the time for reviewing instructions, searching existing data sources, gathering and maintaining the data needed, and completing and reviewing this collection of information. Send comments regarding this burden estimate or any other aspect of this collection of information, including suggestions for reducing this burden to Washington Headquarters Services, Directorate for Information Operations and Reports, 1215 Jefferson Davis Highway, Suite 1204, Arlington, VA 22202-4302, and to the Office of Management and Budget, Paperwork Reduction Project (0704-0188), Washington, DC 20503

1. Agency Use Only (Leave blank)	2. Report Date 2/10/09	3. Report Type and Period Covered: Final Report January 21, 2004 – July 20, 2008

4. Title and Subtitle

High Resolution Anatomic and Elastographic Transrectal Ultrasound for Improved Diagnosis of Prostate Cancer

5. Award Number
W81XWH-04-1-0240

6. Author(s)
John A. Hossack, Ph.D.

7. Performing Organization Name (Include Name, City, State, Zip Code and Email for Principal Investigator)
Biomedical Engineering, MR5 415 Lane Rd
University of Virginia
Charlottesville, VA 22908-0759

E-**Mail:jh7fj@virginia.edu**

8. Performing Organization Report Number (Leave Blank)

9. Sponsoring/Monitoring Agency Name and Address

U.S. Army Medical Research and Materiel Command
Fort Detrick, Maryland 21702-5012

10. Sponsoring/Monitoring Agency Report Number (Leave Blank)

11. Supplementary Notes (i.e., report contains color photos, report contains appendix in non-print form, etc.) NA

12a. Distribution/Availability Statement (check one)
☐ [X] **Approved for public release; distribution unlimited**
☐ Distribution limited to U.S. Government agencies only – report contains proprietary information

12b. Distribution Code
(Leave Blank)

13. Abstract *(Maximum 200 Words)* *(abstract should contain no proprietary or confidential information)*
Existing Digi tal Rectal Exam ination (DRE) and PSA blood te st have inadequate sensitivit y and specificity in the diagnostis of prostate can cer. In this work, we perform ultrasound elasticity imaging, using a slightly inflated latex sheath (to provide a source of moderate pressure) over the transrectal ultrasound probe. The elast icity im age is generated b y cross-correlating successive raw radio frequency image data sets for incrementally increasing pressure. Strain, related to elasticity, can be calculated from the displace ment image. Our second objective is to use a new freeh and 3D acquisition approach to obtain 3D i mage data sets. This approach uses a slightly modified transducer and an im age motion tracking technique. Excellent progress has been ma de with respect to the Statement of Work and three of four total Speci fic Ai ms. A sp ecialized transducer has designed, ordered and received. This transducer provides unsurpassed prostate scanning resolution by virtue of its exceptionally high frequency – up to 14 MHz. Pr ototype phantoms and complete ultrasound test instrumentation has been assembled. Preliminary ultrasound image speckle red uction work has been performed. Preliminary, dimensionally accurate, 3D prostate phantom images have been produced.

14. Subject Terms (keywords previously assigned to proposal abstract or terms which apply to this award)
ultrasound, imaging, elasticity, 3D imaging, image processing

15. Number of Pages

16. Price Code (Leave Blank)

17. Security Classification of Report	18. Security Classification of this Page	19. Security Classification of Abstract	20. Limitation of Abstract
Unclassified	Unclassified	Unclassified	

NSN 7540-01-280-5500

Standard Form 298 (Rev. 2-89)
Prescribed by ANSI Std. Z39-18

Table of Contents

INTRODUCTION

The American Cancer Society estimated that there would be approximately 186,320 new cases diagnosed and approximately 28,660 prostate cancer related deaths in 2008 (AmericanCancerSociety 2008) Currently, patient screening for prostate cancer generally relies on the Prostate Specific Antigen (PSA) blood testing, free PSA testing and the Digital Rectal Examination (DRE). Unfortunately, when using a 'cutoff' of PSA > 4.0 ng/mL and an abnormal DRE, sensitivity, specificity and Positive Predictive Value (PPV) are 38%, 88% and 56% respectively (Crawford, Leewansangtong et al. 1999). An elevated PSA, or an abnormal DRE, when used each in isolation, sensitivity, specificity and PPV are lower (Crawford, Leewansangtong et al. 1999). When the PSA is employed, there is a significant gray area (4 - 10 ng/mL) in which cancers may be missed although the number of negative biopsies is large. Although cancer detection sensitivity, specificity and PPV are improved by combining PSA and DRE (Toubert, Schlageter et al. 1990; Crawford, Leewansangtong et al. 1999) the value of DRE is limited by its subjective nature. DRE is primarily useful in detection of shallow (subcapsular) palpable abnormalities. Systematic multi core biopsy fails to detect clinically detectable cancers in up to 34% of cases (Frauscher, Klauser et al. 2001). There is, however, evidence that as additional biopsies cores are added, sensitivity improves (Taylor, Gancarczyk et al. 2002). This observation has resulted in an increase the number of cores taken during routine examination. Biopsy-based detection sensitivity remains less than ideal. Consequently, there is compelling clinical interest in improved methods for the early diagnosis of prostate cancer with improved sensitivity and specificity. A recent example of progress in the field of prostate cancer detection involves an effort to automate the DRE examination. Savazyan recently described a system for 'mechanical imaging' of the prostate (Sarvazyan 1998). This system comprises a rectal probe that is instrumented with an array of pressure sensing strain gages and a 3D magnetic positioner device. In an *in vitro* trial (Weiss, Hartanto et al. 2001), the new system correctly detected and located 100% of the nodules under examination. This compares with detection rates of 83% and 67% for an experienced urologist and a student respectively. Thus, a significant improvement over the conventional DRE examination has been demonstrated for the *in vitro* case. Another development is the observation that the sensitivity of an ultrasound examination can be improved by the use of a microbubble based contrast agents (Frauscher, Klauser et al. 2001). Frauscher's approach (Frauscher, Klauser et al. 2001) involved the use of contrast agent enhanced Color Doppler that improved the detection of hypervascular regions associated cancer. Prostate cancer was detected by contrast agent assisted ultrasound in 23 of 24 patients known to have prostate cancer. In comparison, conventional ultrasound detected cancer in 17 patients. The contrast agent assisted approach detected cancer in 8 patients with a negative systematic biopsy-based diagnosis. Unfortunately, the cost of the contrast agent is a major issue ($65 per patient). This cost makes up approximately half of the cost of a conventional ultrasound examination and therefore represents a considerable impediment to its widespread acceptance. Other recent publications (Clements 2002; Halpern, McCue et al. 2002) (including one from Frauscher's group) have cast doubt on the true extent of the improvement in diagnostic accuracy obtained by using contrast agents. For example, Halpern was unable to detect cancers in the inner gland and achieved a cancer detection sensitivity of only 42% (Halpern, McCue et al. 2002).

REPORT BODY

The work conducted as part of this Army funded program can be considered as divided into the following key "Aims":
1. Research, design, development and prototype testing of a new transrectal ultrasound transducer, syringe pump and ultrasound instrumentation to facilitate a Synthetic Digital Rectal Examination (SDRE).
2. Research, development and prototype testing of techniques to enable quantitative (dimensionally accurate) 3D reconstructions of the prostate
3. Research, development and test of techniques to improve ultrasound image quality and to facilitate automated (or semi-automated) border detection of lesions
4. Small scale clinical test at the University of Virginia

Excellent progress was made with respect to the four specific aims – with the exception of the fourth aim wherein severe instrumentation problems arose.

The bulk of the reportable image processing work is contained within the Appendix attached.

Progress with respect to the areas are related directly to the committed Statement of Work that was funded:

Aim 1. Design, specify, and have built, a high resolution transducer optimized for imaging elastic inhomogeneities, unsurpassed B-Mode image resolution and possessing integrated 3D capability.
A high frequency (8-14 MHz) transducer array was designed and specified. The transducer was manufactured and delivered by Vermon SA, Tours, France. This specialized ultrasound transducer has two tracking arrays each with 32 elements, a central imaging array with 192 elements and the elements are spaced on a 0.2 mm pitch. This transducer provided, and continues to provide, superb imaging resolution in a transducer housing specially designed for transrectal ultrasound. The transducer has provided the high quality raw ultrasound data as a basis for the subsequent work elements.

Aim 2. Research, development and prototype testing of techniques to enable quantitative (dimensionally accurate) 3D reconstructions of the prostate.
We assembled the apparatus to enable the new approach to transrectal ultrasound based strain imaging in Year 1 and Year 2. We made several custom prostate phantoms using locally developed techniques (Negron, Viola et al. 2002). Using internally made phantoms, we were able to iterate efficiently the design and also to fabricate replacement phantoms at low cost in a timely manner. We tested the tissue elasticity system using both an older 8 MHz transrectal transducer and the newer 14 MHz transducer connected to our Siemens Sequoia ultrasound machine.

Aim3. Research, development and test of techniques to improve ultrasound image quality and to facilitate automated (or semi-automated) border detection of lesions
We made significant progress with respect to two specific aspects of image processing. Firstly, we made progress with respect to speckle reduction. This worked is described in detail in the body of this report. Secondly, we developed new algorithms for segmenting ultrasound data – mostly described in published papers included as an appendix attached to this document.

Aim 4. Small scale clinical test at the University of Virginia
We worked to complete both UVA and DoD Human Subjects Protection documentation in place for the small scale human pilot study. We planned to conduct a small study in the final six months of the project – per a second 6 month no cost extension granted in January 2008. Unfortunately, the ultrasound scanner required for this research (Siemens Sequoia 512) is very unreliable and frequently "dead" and it has proven exceptionally difficult to repair due to lack of

interest on the part of Siemens and due to staff turnover at Siemens resulting in severe lack of continuity with respect to expert engineering support. Ultimately, Siemens have threatened to remove the scanner since they consider the underlying research agreement to have expired. We continue to strive to have the Sequoia repaired and have its status resurrected as an approved research agreement loaned asset since it forms a core resource within our research facilities.

Detailed report:

Phantom

A purpose-built prostate phantom was designed using the method described in Negron et al. (Negron, Viola et al. 2002). A simulated lesion (approximately 0.3 ml) was formed inside of an egg-shaped tissue region mimicking a prostate. A cylindrical cavity (20 mm in diameter) was formed to mimic the anal opening and to allow access for the transrectal transducer. A hypoechoic gel component surrounds these three components. (Strictly speaking, the surrounding gel should be echogenic too but the lack of echoic inclusions is immaterial in our phantom studies.) The lesion is made of 17% (by weight) acrylamide gel; the tissue and exterior component are made of 5% acrylamide gel. Thus, the lesion is perceptibly stiffer (approximately 10 times stiffer) than both the egg shaped tissue region and the exterior gel component. A similar concentration (by volume) of Sephadex was added to both the lesion and the tissue, resulting in similar ultrasound image intensity in these two structures (The lesion was made slightly brighter than the tissue in order to assist navigation during scanning.) A B-mode ultrasound image of the prostate is shown in Fig. 1. The lesion in the image is almost isoechoic. This phantom is similar to ones we have made since the beginning of the project.
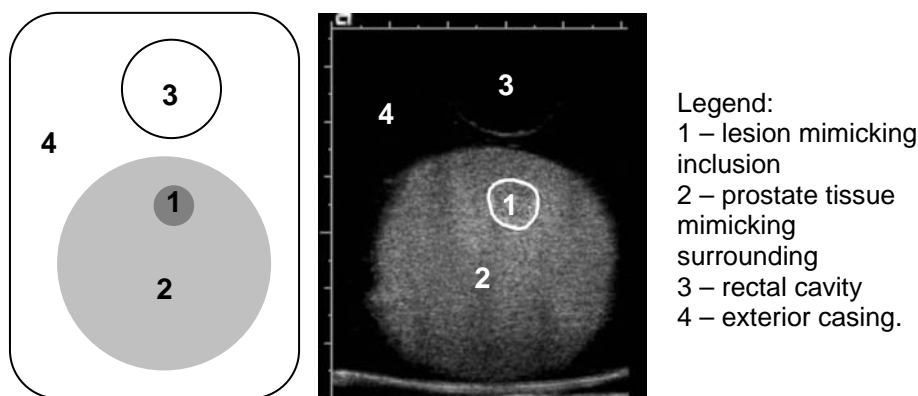

Legend:
1 – lesion mimicking inclusion
2 – prostate tissue mimicking surrounding
3 – rectal cavity
4 – exterior casing.

Fig. 1. Left: Schematic of the transrectal design of prostate phantom. Right: An ultrasound image of the phantom.

Transducer

Vermon SA, Tours, France fabricated an 8-14MHz transrectal transducer to our specification. This was delivered in Q1 2005. Most prostate transducers used today in premium ultrasound scanners use a tightly curved array placed on the end of the transrectal probe. Thus, these probes have limited aperture contribution to image resolution at any particular point in the image field. However, this new transducer has a linear array format and hence has a longer available aperture that results in finer lateral resolution. Thus, we believe that this transducer's imaging resolution is practically unmatched in the field of prostate ultrasound. Image resolution is approximately 0.2 mm lateral and 0.1 mm in the axial (range) dimension. The array pitch is 0.2 mm. There are 192 elements in the imaging array and 32 elements in each of the two perpendicular tracking arrays that provide the

transducer with "I-Beam" 3D tracking (Hossack, Sumanaweera et al. 2000). This form of 3D tracking yields approximately 4.6% accuracy at the two standard deviation level. (95% of measurements will be within 4.6%.) The I-Beam transducer is also uniquely matched to the transrectal prostate ultrasound application for the following reasons: a) the transrectal probe with the tracking mechanism near the transducer minimizes numerical ill-conditioning that may arise if the means of tracking is separated from the imaging array, and b) the I-Beam transducer estimates the relative tissue motion rather than absolute tissue motion, which enables efficient and accurate measurements even if there is patient motion of the type that can defeat a 3D system that uses a fixed origin for 3D positioning (eg. Magnetic-based, optical-based, or articulated arm-based positioner.)

The newly developed transducer required new software drivers to be developed to enable it to "run" on our Siemens Sequoia research scanner. One graduate research assistant (Yinbo Li) spent the summer of 2005 at Siemens Engineering in Mountain View, CA, developing the required software with assistance from Siemens Engineering Staff – primarily Greg Holley. Siemens assisted with costs associated with this development. Siemens Engineering also performed ultrasound output intensity measurements to verify that the transducer satisfies current FDA regulated intensities (primarily that Mechanical Index (MI) <= 1.9). While the transducer was having software development, we also took advantage of the opportunity to add a contrast agent imaging mode for potential future work in this area. Contrast Pulse Sequences (Phillips 2001) was implemented on the transducer. It is intended that this will enable future work that might be based on measuring perfusion in prostate or locating the presence of molecular targeted ultrasound contrast. These applications are beyond the scope of the currently funded work and will not be pursued without future funding and any requisite permission.

The transducer, system and phantom are assembled into a complete working 3D scanning / elastographic system by adding a latex sheath over the transducer (secured with elastic bands), Tygon™ flexible plastic tubing and syringe pump to controllable inflate the sheath with plain tap water. When these components are assembled we have the basic apparatus for the "Synthetic Digital Rectal Examination" described in the proposal. The programmable syringe pump is a Harvard Instruments PHD 2000, (Harvard Apparatus, Holliston MA). This pump enables automatic water inflation and can generate a quasistatic stress and produce as uniform tissue deformation as possible. A syringe volume of 60 ml was chosen to provide sufficient water to compress and deform the rectal wall thus providing an optimal tissue strain. This volume is also appropriate in that when used in a clinical setting, the ultimate size of the syringe makes the water injection process safe in that the syringe is emptied before any patient injury could be anticipated. We have recently discovered that other research groups have also adopted a somewhat similar balloon inflation method but that these earlier efforts use a manually operated syringe (Lorenz, Sommerfeld et al. 1999; Alam, Fellepa et al. 2004).
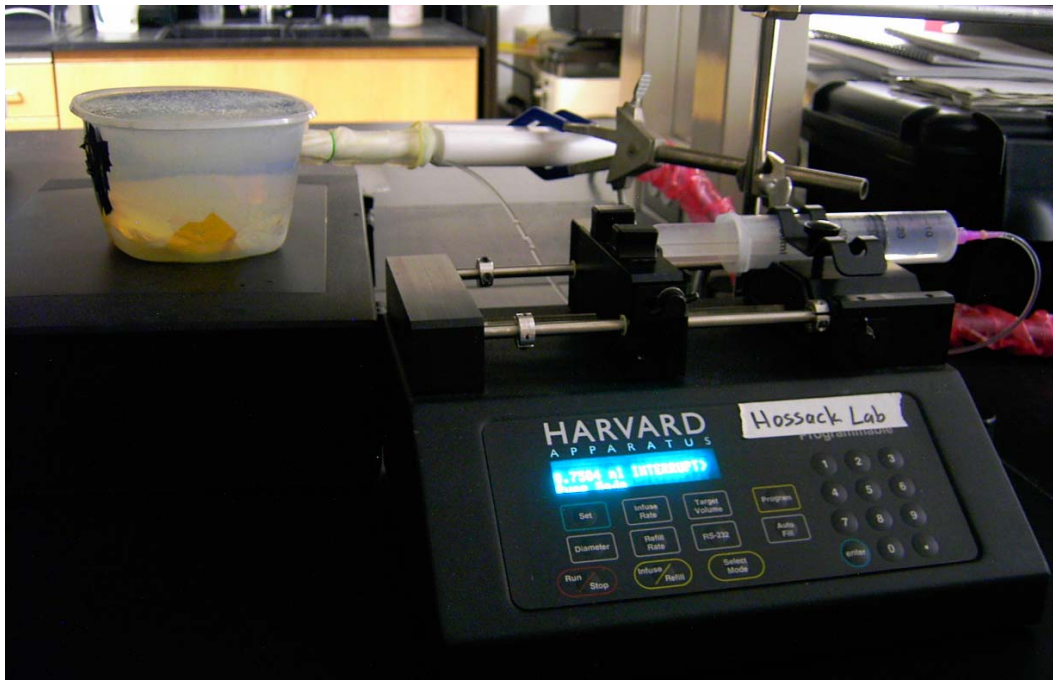
Fig. 2. The transrectal transducer is covered with a latex condom. Water was inflated by the syringe during imaging
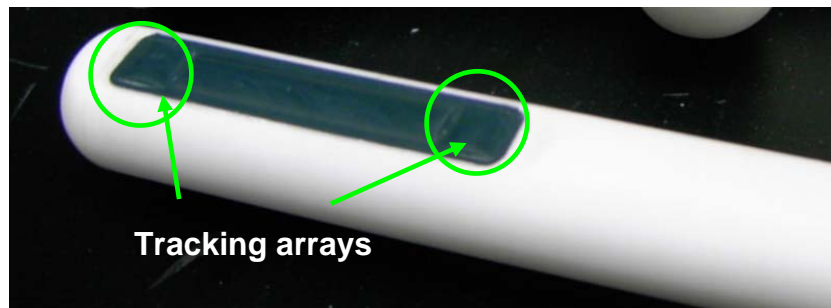

Fig. 3. I-Beam transducer – possessing a main imaging array in the center and a tracking array in each end

Five elevational slices each comprising of 100 Sequoia 14 MHz In-phase/Quadrature (I/Q) data frames were acquired during the in-vitro experiment using an incremental strain between the consecutive frames of 0.04 %. Total applied strain between the first and the last frame was approximately 4 %. This strain is broadly in accordance with the degree of strain that has been found to be optimal for strain imaging (Lubinski, Emelianov et al. 1999).An example B-mode image obtained by the transrectal I-Beam transducer is shown in Fig. 4.
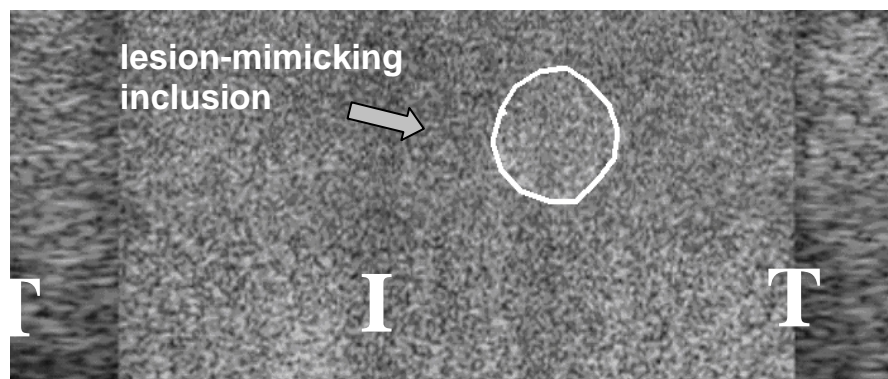
Fig. 4. A B-mode image acquired with the I-Beam transrectal transducer from the prostate-mimicking phantom, showing the layout of image planes formed by 'Tracking' arrays and 'Imaging' array. 'T' – tracking array, 'I' – main imaging array. Delineated is a lesion-mimicking inclusion.

Elasticity Calculation and 3D Reconstruction

The acquired IQ data were filtered using a low-pass filter to reduce jitter, electronic noise, and out-of band noise. Six pairs of frames with differential strain of 2% were tracked using a time-domain cross-correlation technique. Signal "companding" or stretching was employed to maximize the cross-correlation coefficient between the pre- and the post-compression frames. Companding techniques improve contrast to noise ratio of the strain images. This improvement is desirable as the prostate lesions are known to be twice or at most thrice stiffer than the prostate. Sub-sample precision was obtained in the delay estimates by using a quadratic fit to the cross-correlation function. A search window of approximately 5 wavelengths was used for time-delay estimation. Lateral motion was tracked using the technique described by Lubinski et al.(Lubinski, Emelianov et al. 1996). Displacement estimated from these six different renditions were averaged to eliminate uncorrelated random noise. Strain estimates were then obtained by taking the local gradient of the displacement image (in axial direction). The above process was repeated by sweeping the transducer in the elevational direction and six elevational slices were obtained. In the elevation direction, the inter-slice distance was estimated with a block matching approach based upon the minimum sum of absolute differences (MSAD) algorithm of the I-Beam 'Tracking' data. The inter-slice distance was found to be slightly larger in the deeper portion than in the shallower portion, indicating that the transducer was rotated by small angles between measurements. In the measurements, the slices were sampled with an interval no greater than 2 mm, and the rotation angle increments were less than 2 degrees in order to ensure that the elevational motion could be accurately tracked. Once the elevational motion of these blocks was calculated, the acquired image slices were interpolated on to a regular 3D grid in Matlab enabling 3D volumes to be rendered

Figure 5 illustrates the lesion detection process. The elasticity reconstruction algorithm was tested on the phantom data. The elasticity reconstruction process for the detection of prostate cancer is complicated than the elasticity reconstruction process of the breast cancers. Unlike the boundary conditions for breast cancer detection, the boundary conditions for prostate cancer detection are non-trivial. The effect of which is obvious in the reconstructed displacement and the strain images. These non-uniform boundary conditions result in non-uniform and non-symmetric internal displacements, which can be seen in the axial displacement image. This results in strain concentration artifacts along the top most boundary of the strain image. The non-uniform boundary conditions also cause a non-linear decay in strain with increasing depths. The isolated saturation of strain in the lower quarter of the strain image is due to the out-of-plane motion, which cannot be tracked with linear array transducer. Two-dimensional arrays may probably solve these problems, which in turn may result in substantial improvement in the quality of strain images. It is also important to note that no post-processing was done on the strain images. In spite of the unique challenges associated with the elasticity reconstruction process of the prostate
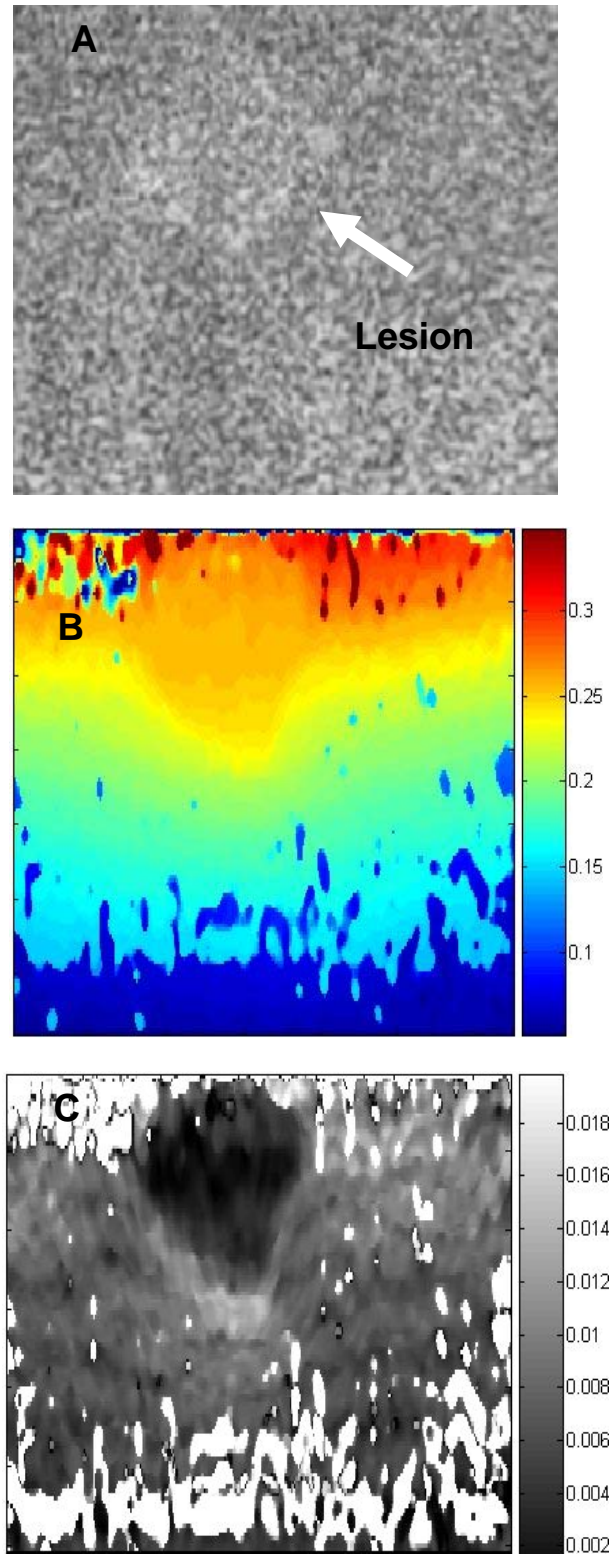
Fig. 5. The lesion detection process. The lesion is barely identifiable in the original B-mode image (A). A displacement image is illustrated in (B). The lesion is clearly identifiable in the strain image (C).

The 3D volume of the detected lesion was calculated after segmenting the 2D contour in each slice and estimating the inter-slice distance. A multiple slice view and a 3D surface view of the identified lesion were rendered based on the 3D dataset as shown in Fig. 6. The volume

measured in the elastography and 3D reconstruction is approximately 339±11 mm^3 less than 15 % volumetric error from the volume of 300 ±30 mm^3 measured using Archimedes principle.
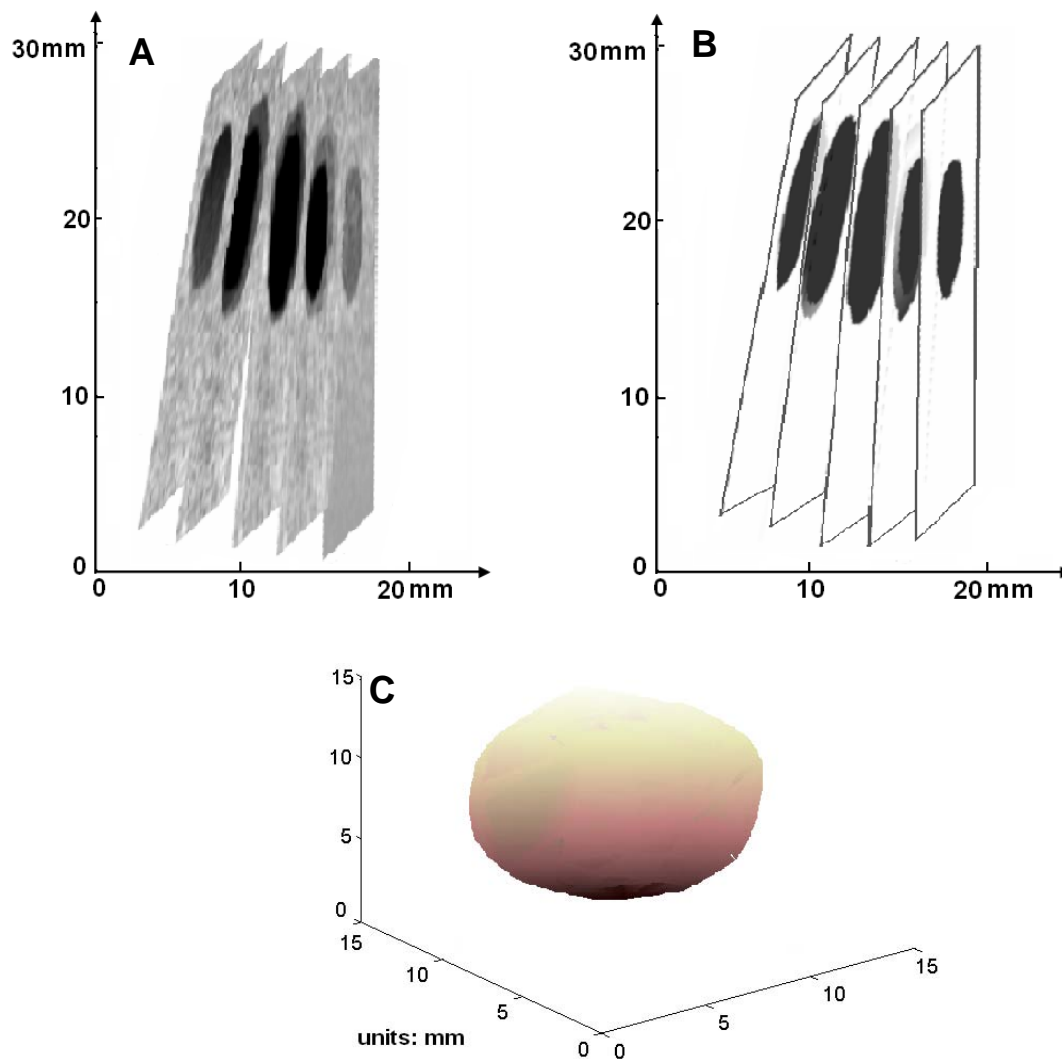

Fig. 6. 3D reconstruction of the lesion. A: The multiple 2D image slices acquired were rendered in three dimensions. The lesion was shown darker than surrounding tissue. B: The multiple slices of elasticity images with the detected lesion shown in black. C: The prostate lesion detected from the ultrasound images. The lesion was segmented from the surrounding tissue and its 3D surface was rendered.

The results shown above indicate that the finer resolution of the new higher frequency transducer yield superior imaging and 3D reconstruction results. The new transducer operates at up to 14 MHz. The transducer previously used (as reported last year) used 8 MHz imaging and a similar aperture dimension.

Image Processing and Quantification
We have progressed to a accurate 3D surface rendering from 2D slices by implementing a 3D gradient vector flow (GVF) snake algorithm (Xu and Prince 1998). The 2D and 3D GVF snake algorithm relies on the edges to be well delineated and contrast between the various regions to be well defined in each 2D ultrasound slice to produce a surface that resembles

the actual scanned object. In ultrasound, images are affected by a granular pattern commonly known as speckle. Before an accurate 3D surface rendering can be attained a preprocessing despeckling step is needed to reduce the variances in pixel values within homogeneous regions while contrast between distinct regions are concurrently enhanced. We have evaluated a wide variety of well known methods such as the Nagao and Matsuyama filter (Nagao and Matsuyama 1979), the Lee filter(Lee 1980), the Frost *et al.* filter (Frost, Stiles et al. 1982), the Kuan *et al.* filter (Kuan, Sawchuk et al. 1985), the adaptive weighted median filter proposed by Loupas *et al.*(Loupas, McDicken et al. 1989), the Wiener filter (Kailath 1976), the SRAD proposed by Yu and Acton (Yu and Acton 2002), and a novel stochastically driven method design specifically for 3D surface rendering from 2D slices of the prostate and other organs. The method we develop specifically for the task of this grant is a stochastically driven compression filter called the squeeze box filter (SBF). Our quantitative evaluation using a Field II (Jensen and Svendsen 1992) simulated B mode ultrasound image with contrast enhancement performance determined by a modified Fisher discriminant has determined that the newly developed SBF method outperformed the other methods and is exceptional in providing the needed intra-region reduction in variance and inter-region contrast enhancement with computational efficiency. In Figs. 7 and 8, we show the results of SBF and SRAD applied to a Field II simulated image. It is visually evident that the bright and dark disks in the SBF result is more pronounced than in the SRAD image. In Figs. 9 and 10, we show the SRAD and SBF results, respectively, using an ultrasound image of a phantom. Again, it is evident that the results of the simulation are up held with the results of the actual ultrasound phantom image in that edges are well preserved and contrast is better enhanced with the SBF than with SRAD. In Figs. 13, 14, and 15, we show the 3D surface, the side view, and the bottom view, respectively, of the rendering we attained from a sequence of scans we acquired of an egg phantom. The sequence consists of acquiring a 2D slice every millimeter along the long axis of an egg phantom. We processed each slice with the SBF despeckling method. The original unprocessed middle slice is show in Fig. 11. The SBF processed middle slice is shown in Fig. 12. The 3D rendering was attain by SBF processing each slice then applying a 3D GVF snake to attain the final results shown in Fig. 13, 14, and 15. It is very evident that our method captured the essential size and shape of the egg phantom. The volume estimate we attained for the object enclosed by the surface was only 10% off of the actual volume of the phantom.
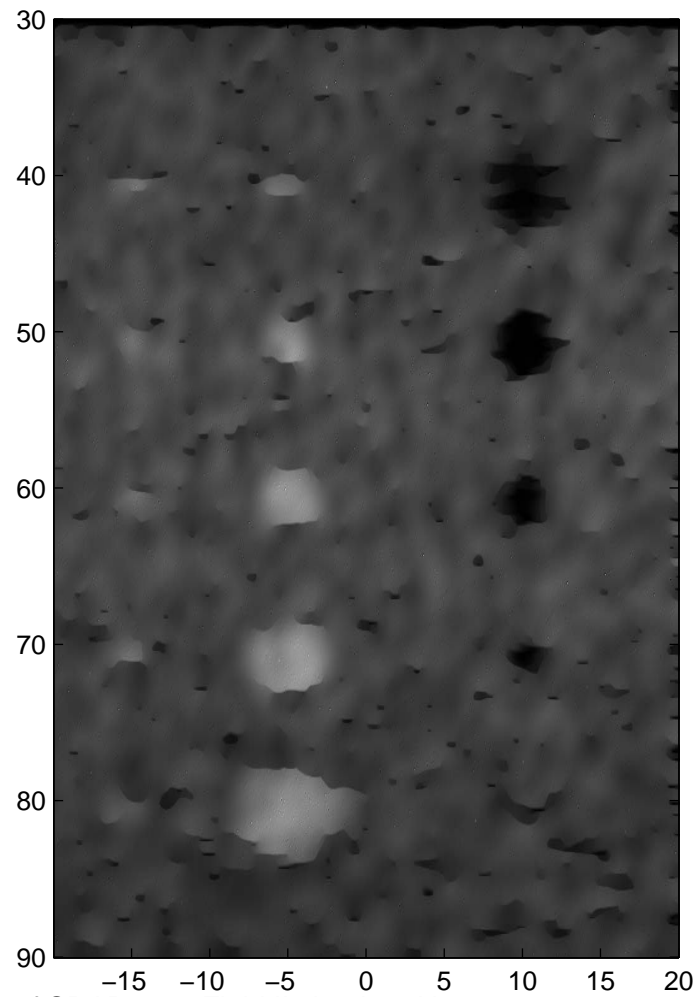
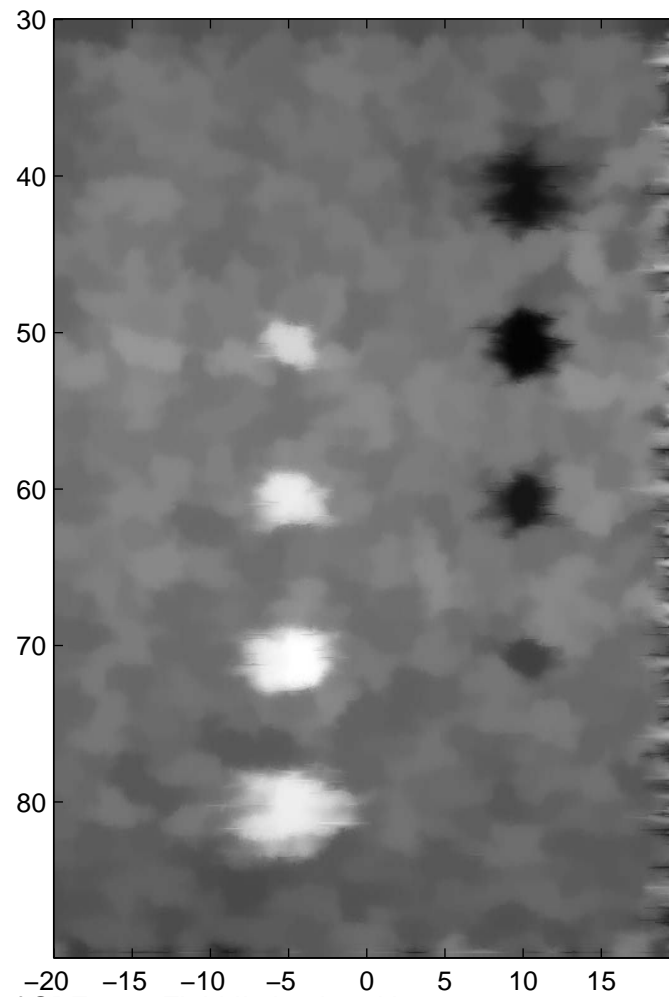Figure 7. The result of SRAD on a Field II simulated image.

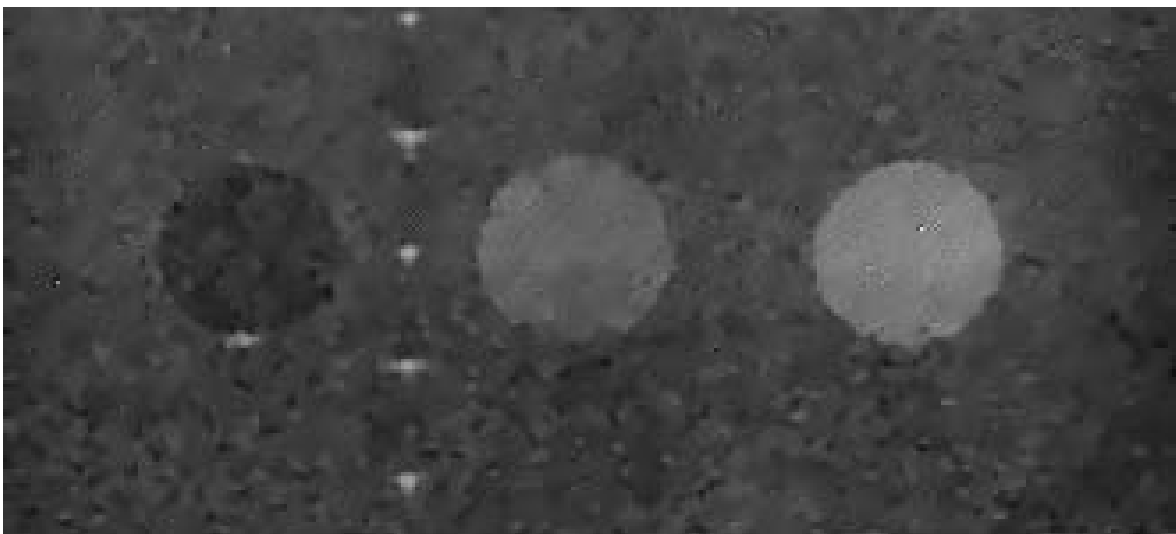Figure 8. The result of SBF on a Field II simulated image.

Figure 9. The result of SRAD on an actual ultrasound image of a phantom.
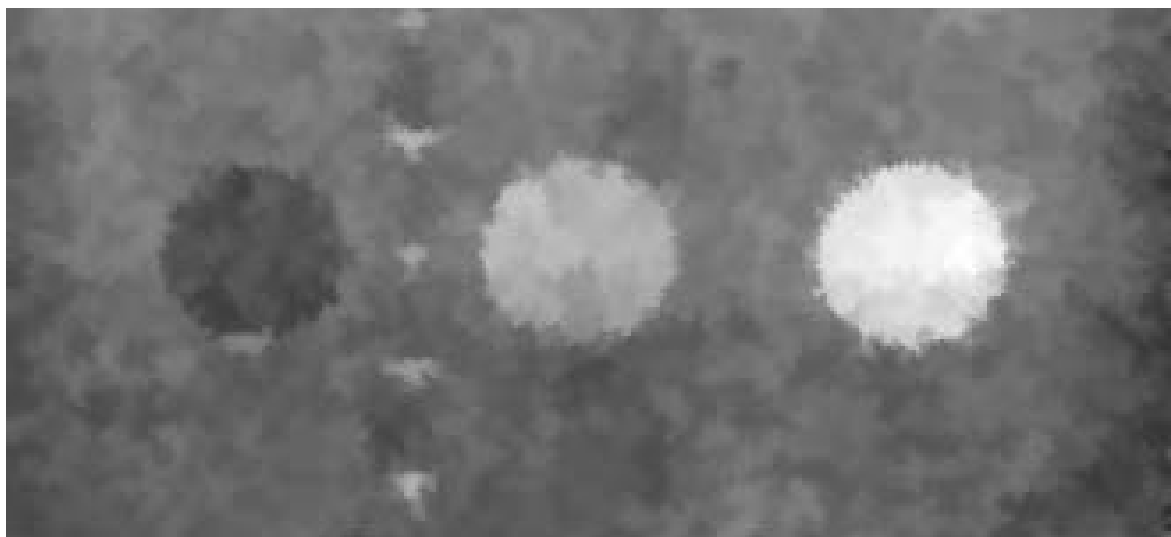
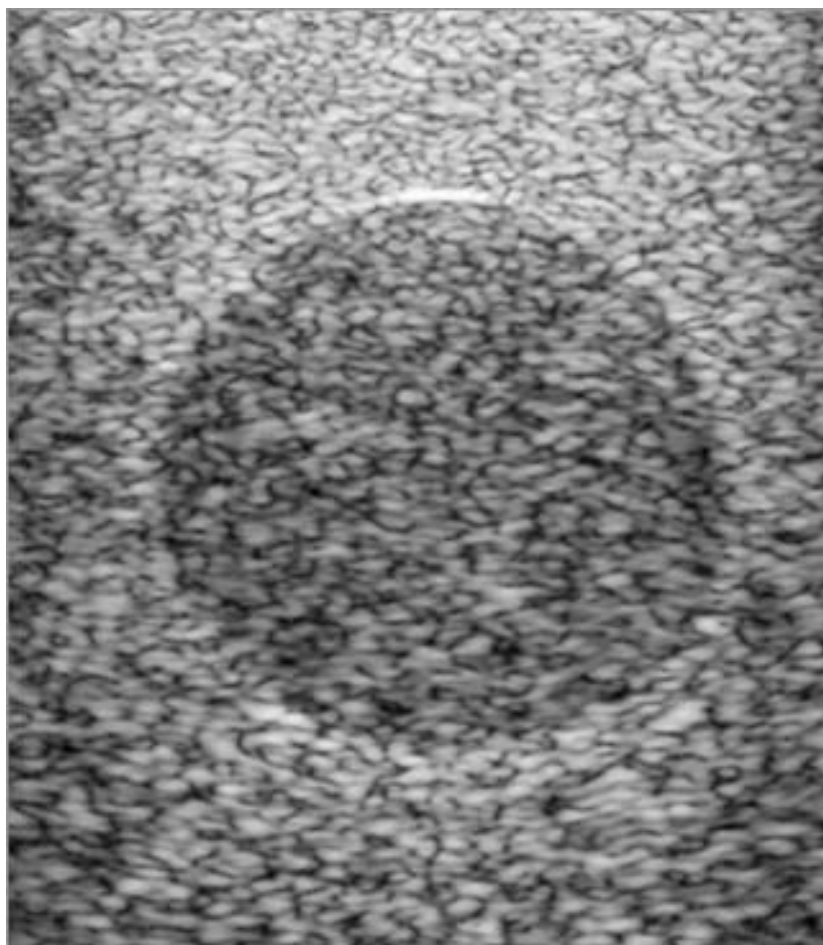Figure 10. The result of SBF on an actual ultrasound image of a phantom.

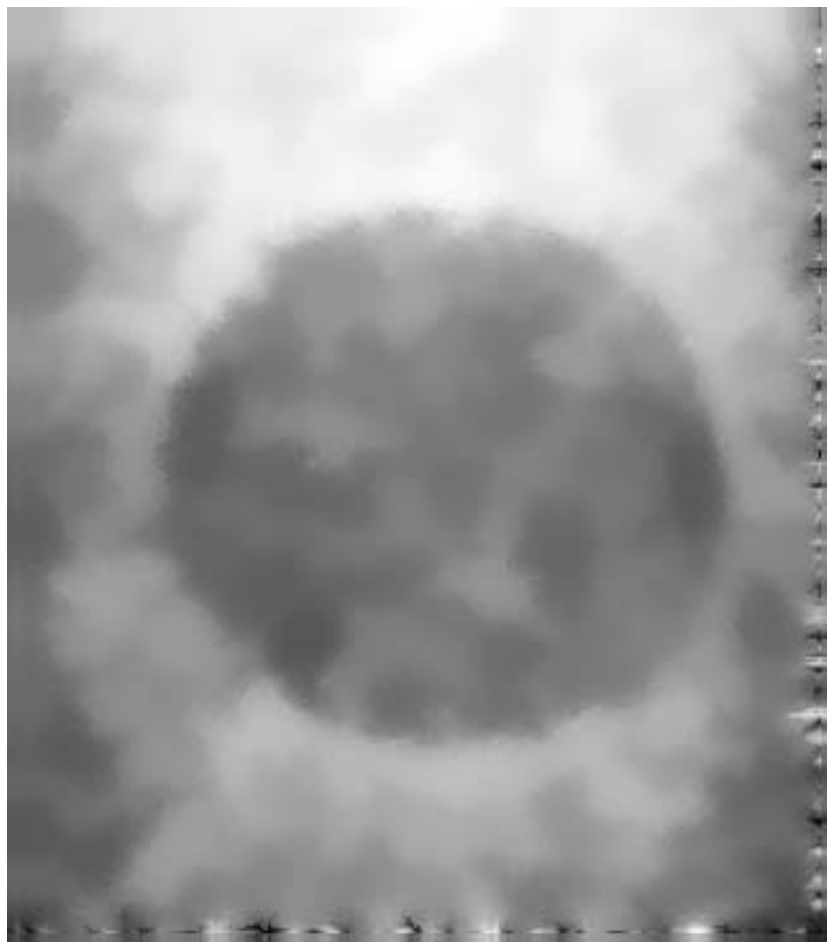Figure 11. Unprocessed middle slice of the egg phantom.

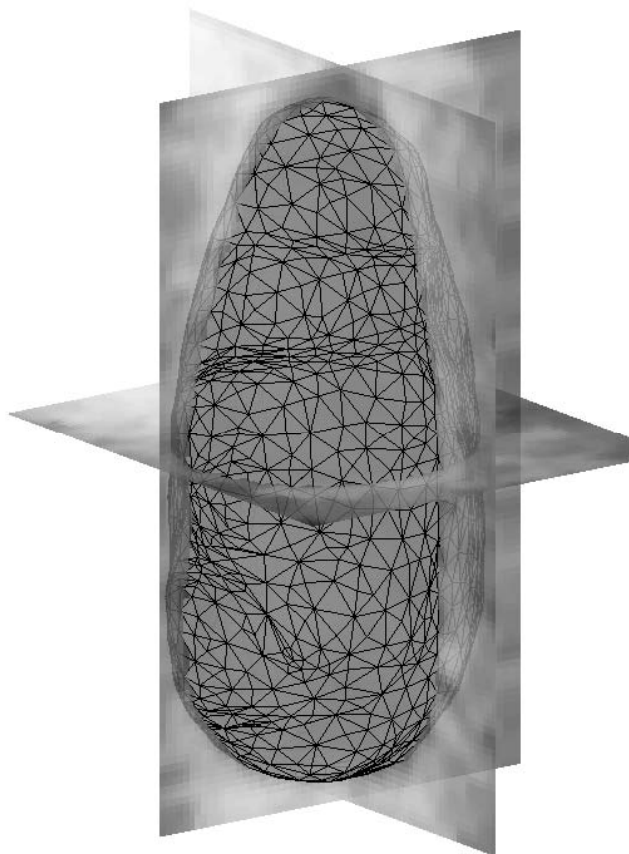Figure 12. SBF processed middle slice of the egg phantom.

Figure 13. 3D surface found by the 3D GVF with slices preprocessed by SBF.
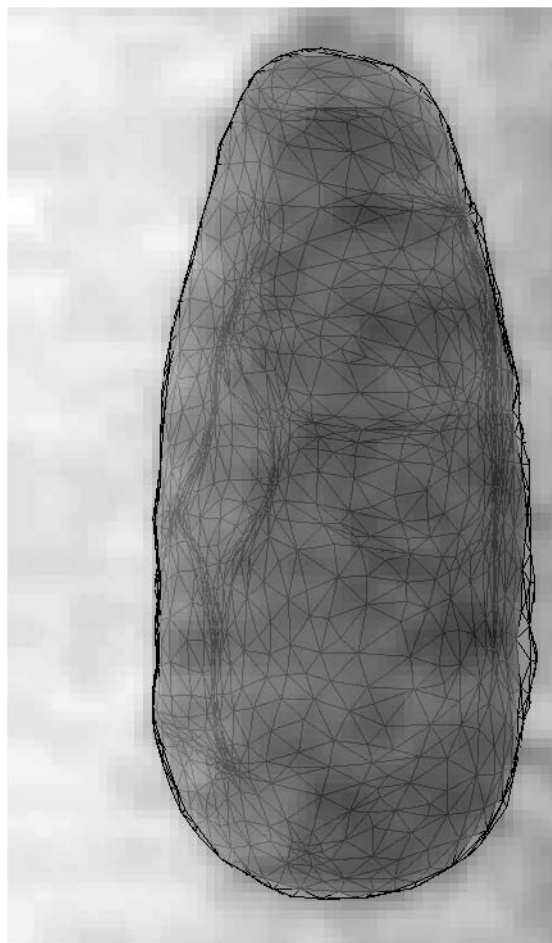
Figure 14. Side view of the surface rendered by the 3D GVF snake
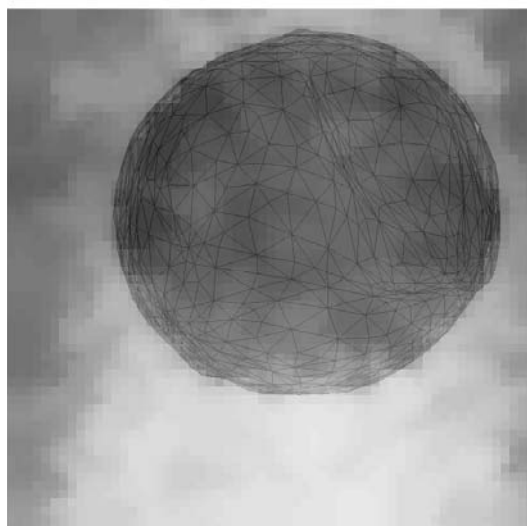with slices preprocessed by SBF.

Figure 15. Bottom view of the surface of the egg phantom
rendered by the 3D GVF snake with slices preprocessed by SBF.

Multi-resolution hybrid strain estimator

Time delay estimation has been extensively reported in the literature as an effective method to estimate blood flow (Kasai et al. 1985) and tissue motion (Chen et al. 1992). In the field of elastography, O'Donnell et al. (1994)) have used the zero-crossing of the phase of the complex cross correlation function (base band signal) to estimate tissue strain, whereas Konofagou et al. (2000a) have used shift in the power spectrum of the pre- and post-compression echo RF signal to estimate tissue strain. Bilgen (1999) has reported a wavelet based direct strain estimator (no gradient operation) for elastography. In this section, we describe a multistage hybrid adaptive displacement (and strain) estimation algorithm. Figure 1 illustrates the complete flow chart of this strain estimation algorithm, which is elaborated in the following paragraphs. In strain estimation, cross-correlation between pre- and post-compression signals is maximized when two signals are jointly stationary. In addition, if the time-bandwidth product is large and the shifts in the signal are small, cross-correlation is an efficient estimator of displacement (hence strain) and in the limit achieves the Cramer-Rao lower bound on variance (Walker and Trahey 1995). However, in practice, pre- and post-compression signals are jointly non-stationary. Hence, signal companding (Chaturvedi at al. 1999) or stretching (Céspedes and Ophir 1993) is frequently used to improve image quality. However, for global stretching to be effective, an *a priori* estimate of applied tissue strain is required. In conventional elastography, a calibrated and computer controlled motion stage is used to apply an external displacement, it accurately determines the applied displacement at the top surface of the object being compressed due to uniform compression. Hence, the applied strain at the top of the compressed object is known *a priori*. In hand-held and trans-rectal prostate elastography, applied displacement cannot be guessed *a priori* as the applied compressions are not calibrated or controlled. In addition, the strain induced in the compressed object decays or attenuates with depth, and is governed by non- uniform[1] boundary conditions.

---

[1] When the compressor plate is smaller in dimension than that of the co mpressed homogeneous object, the stress distr ibution in the object is non-uniform and is referred to as non-uniform boundary condition at the object boundary (Shapo et al. 1996,).

Figure 1: Flow chart of the new strain estimation algorithm. Note: dotted lined-rectangular boxes denote first-stage (I), whereas, dashed lined-rectangular boxes signify second-stage (II), and solid lined-rectangular boxes represent third-stage (III).

Hence, uniform global stretching in the first stage of any adaptive strain estimation algorithm (Srinivasan et al. 2002b) may produce sub-optimal results. Also, when applied strain is large (> 2%, for a ~4 cm deep prostate tissue imaged at 12 MHz), the induced displacement is sufficiently larger than the wavelength corresponding to center frequency and may introduce ambiguity in peak detection of the cross-correlation function obtained by tracking the pre- and post-compression RF data. Hence, in the first stage of our algorithm, we demodulate the RF data and track the envelope of the pre- and post-compression echo RF frames to yield average "first-guess" strain estimates over the tracking window-W. The window, W, is the spatial length of the kernel over which the pre- and the post-compression signal cross-correlation is carried out. The window in this stage is larger than in the subsequent RF tracking stages to obtain

estimates with higher SNR. The displacement obtained from this stage is referred to as the first stage axial displacement (^1D_a), where superscript '1' denotes the stage and subscript 'a' denotes the displacement type (axial

In the second stage, a polynomial curve[2] is fitted to the estimated local strain profile over an A-line, and the corresponding A-line is stretched by the curve-fitted first-stage strain. Srinivasan et al. (2002b) stretched the post-compression data globally by the average applied strain, whereas Chaturvedi et al. (1999) compressed the pre-compression data by the average tissue strain. In either case, the first stage did not take into account the local variations in tissue contrast. In addition, both algorithms require an *a priori* estimate of the applied strain. In the proposed algorithm, signal stretching is performed locally over a tracking window on every A-line, taking account of the local variation in tissue elasticity without any *a priori* knowledge of the applied tissue strain. Lateral displacement (^2D_l) is estimated by performing lateral tracking (Konofagou et al. 2000b). The pre- and the stretched post-compression echo RF data are then tracked to yield a local strain estimate over the search window. The axial displacement estimated in this stage is added to the first stage axial displacement and the resultant axial displacement is referred to as the second stage axial displacement (^2D_a).

The third stage is used to estimate residual strain. In the third stage, the original un-stretched post-compression RF data are stretched locally over a tracking window using the estimated second-stage strain. The stretched post-compression data are then tracked with the pre-compression data to yield residual axial displacements. The lateral displacements are obtained by tracking the A-lines laterally. When performing lateral tracking, the search window in the pre-compression data is tracked with the corresponding window on adjacent A-lines in the post-compression data. The maximum cross-correlation coefficients over these windows are estimated and a cosine curve (cosine interpolation) (Céspedes and Ophir 1993) is fitted to the data points. The shift in the peak of this curve in the transverse (lateral or azimuthal) direction yields the lateral displacement of the local post-compression window. The axial and lateral displacements estimated in this stage are added to the second stage axial and lateral displacement to yield the final axial (^3D_a), and lateral displacements (^3D_l). The gradient of the axial displacement image yields a strain image, but gradient operator is a high pass operator and amplifies noise. A least square estimator may be applied to a displacement image to produce a smooth elastogram, but the losses in tissue contrast and resolution may be substantial (Kallel and Ophir 1997). A staggered strain operator (Srinivasan et al. 2002a) limits noise amplification and provides smooth elastograms while minimizing the loss in contrast and resolution. Hence, in the last step of this algorithm, we apply staggered strain estimation technique to the final stage axial displacement image to generate a final stage elastogram. In principle, the staggering estimator performs a band-pass filtering operation partially mitigating the noise-enhancing effect of the high pass filtering resulting from the gradient operator.

---

[2] The estimated first stage strain profile is interpolated using cosine interpolation to match the sampling rate of the RF data.

3D Elastographic simulation framework

An elastographic simulation framework similar to that proposed by Nightingale (Nightingale, Nightingale et al. 2000) (2000) and Patil (Patil, Krouskop et al. 2008) was used to in this work. Patil et al. had used a 3D shift-invariant convolution model for generating the pre- and post compression echo RF data. In this work, we have used a more realistic Field II simulation model (Jensen and Svendsen 1992) for echo RF data generation. Most FEA simulations performed by Patil et al. were restricted by the assumption of uniform boundary conditions, which is not strictly valid for transrectal prostate elastography. In this work, all FEA simulations were performed with non-uniform boundary conditions. Figure 2 illustrates the flow diagram of the simulation framework used in this work. ANSYS (Canonsburg, PA), a finite element analysis (FEA) simulation software package, was used in this work. Arbitrary regions of interest (ROI's) can be created within the FEA model by changing the local material properties (shear modulus, material density etc.). A fine FEA mesh (approximately 13 FEA nodes per resolution cell) results in accurate parameter estimation (3D internal displacement, in this case). Boundary conditions (applied displacement) can be applied to an object surface, an object element, or a node of the object element (after meshing). The internal object deformation due to the applied displacement is then estimated by solving the associated partial differential equations numerically. In this work, a preconditioned conjugate gradient iterative solver was chosen to perform numerical simulations (Elman and Agron 1989). This solver was chosen because it provided similar performance as compared with the other solvers (within ANSYS) at a relatively small computational time. A grid of scatterers was defined over the 3D ROI of the simulated object (48 scatterers per resolution cell (Walker and Trahey 1995)). The post-compression scatterer position was simulated by applying the 3D displacement field obtained from the FEA software to the scatterers.
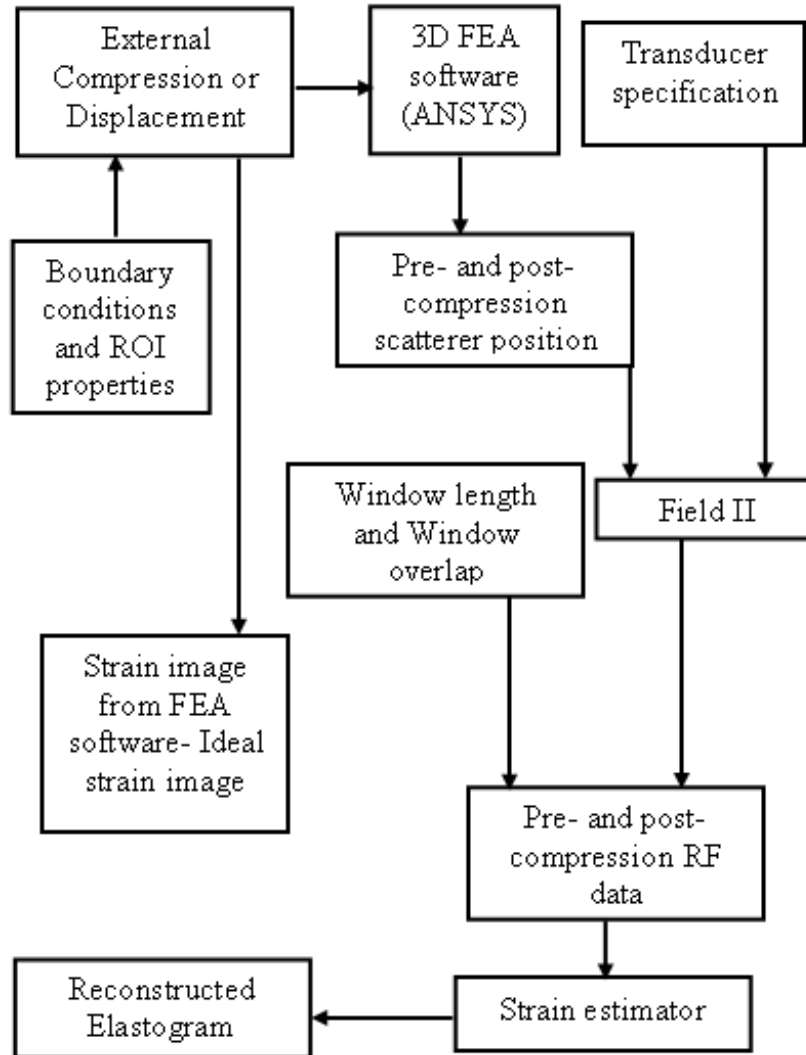
Figure 2: 3D elastographic simulation framework .

It is worthwhile noting that the FEA simulations accounted not only for translational but also for rotational motion of an object due to any arbitrary boundary condition. Thus, realistic tissue motions can be simulated for arbitrary boundary conditions and arbitrary object shapes. Field II simulations were used to generate the pre- and post-compression echo RF data. The generated pre- and post-compression data can be tracked using different displacement (strain) estimation algorithms to generate a strain image. In this work, we used the strain estimation (signal processing) algorithm detailed in section 2.

Performance evaluation of the strain estimator using 3D elastographic simulations and experiments

A. Simulations

Elastographic simulations were performed using the framework described in section 3. Table 1 lists the simulation parameters used for performing various simulations described in this section. **Table 1 Simulation parameters .**

Entity	Value
Dimensions of background	40x40x40 mm cube
Modulus ratio of inclusion and background	3
Approximate diameter of the inclusion	10 mm
Center frequency of scan	12 MHz
Sampling frequency	80 MHz
System SNR	30 dB
1D linear array	192 elements, 0.2 mm pitch
Focus	20 mm
Fractional bandwidth	40%
Window length (W)	2 mm
Overlap	90%

A cube (40 x 40 x 40 mm) enclosing a spiculated inclusion (10 mm diameter) was used as a mechanical model to simulate the background and the lesion (Figure 3). The embedded inclusion (Young's Modulus=12 KPa) was simulated to be three times stiffer than the background (Young's Modulus=4 KPa). A uniform cube was used for the SNR study. The cubes were compressed axially from the top and assumed to be rested on a fixed surface such that their motions in the lateral and elevational directions were unconstrained (slip conditions). The cubes were compressed along the elevational axis of symmetry using a compressor plate (40 x 3 mm- lateral elevation plane) and the transducer array was placed over the compressor plate. The surface area of the compressor plate was smaller than the surface area of the top of the cube to simulate non-uniform boundary conditions at the top surface of the cube (Figure 3). This results in non-uniform stress distribution through the depth of the tissue and consequently causes strain decay. The cube was subjected to a range of applied strain (0.5-10%). ANSYS was used to perform these simulations. The transducer was focused at 20 mm (range or axial direction). RF data were generated using the 3D elastographic simulation framework as described in section 3
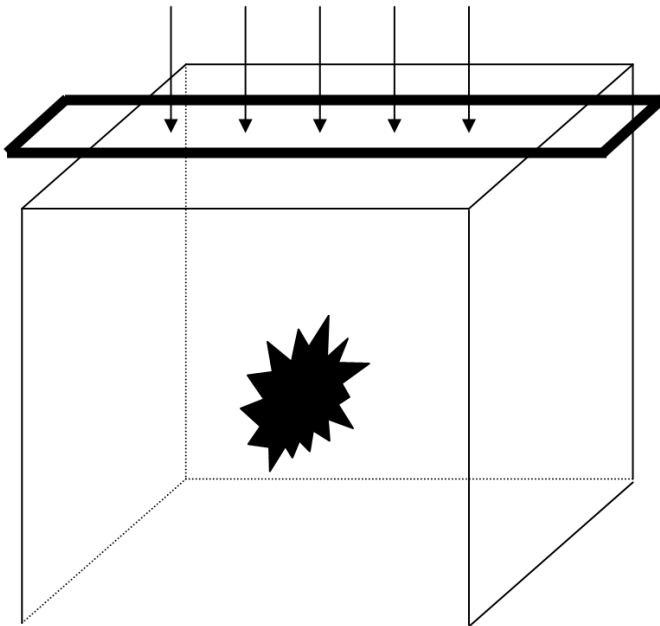

Figure 3: Schematic of the simulated phantom and imaging array used for CNR$_e$ study. The cube is 40x40x40 mm and the compressor plate is 40x 3 mm.

The generated pre- and post-compression RF data were tracked using: 1) the proposed algorithm, 2) the algorithm proposed by Srinivasan et al.(Srinivasan, Kallel et al. 2002), and c) 1D RF data tracking using uniform global stretching (Cespedes and Ophir 1993). Signal-to-noise ratio (O'Donnell, Skovoroda et al. 1994) and contrast-to-noise ratio (Bilgen and Insana 1997) were used as metrics for comparing the above listed tracking algorithms. Figures 4 through 7 illustrate the first, second and final stage elastograms obtained using the proposed algorithm. Figure 8 illustrates the numerical strain image obtained from 3D FEA simulation

Figure 4: First stage elastogram (Left) and axial displacement image (Right). The field of view is 40x40 mm. The images were obtained using parameters specified in Table 1.
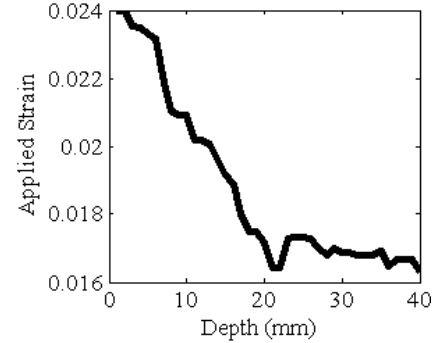

Figure 5: Strain profile over an A-line in the elastogram (Figure 4-Left) obtained by the B-mode tracking.
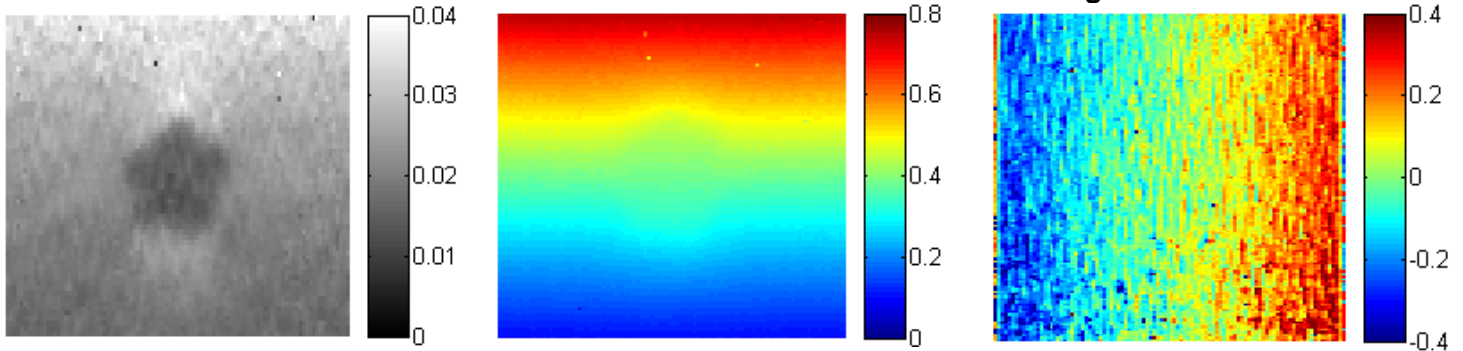

Figure 6: Second stage elastogram (Left), axial displacement image (Center), lateral displacement image (Right). The field of view is 40x40 mm. The images were obtained using parameters specified in Table 1.
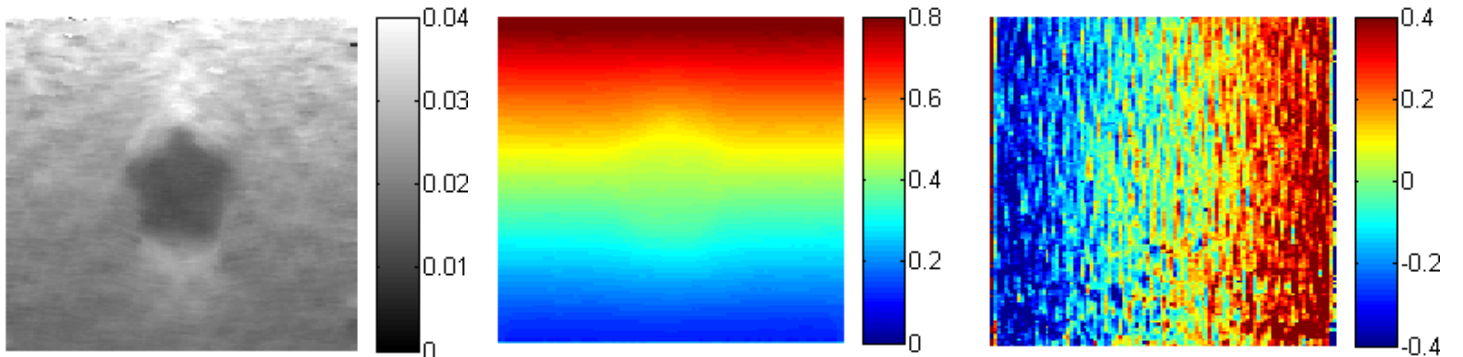

Figure 7: Final stage elastogram (Left), axial displacement image (Center), lateral displacement image (Right). The field of view is 40x40 mm. The images were obtained using parameters specified in Table
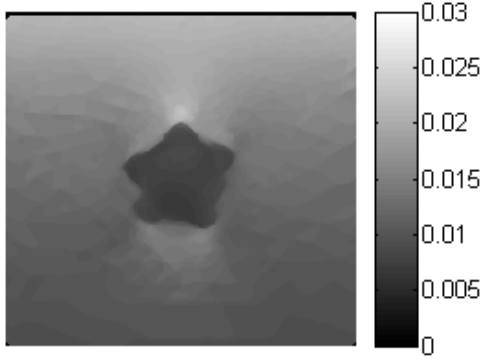
1.

Figure 8: Ideal strain image obtained from the FEA simulations. The image was obtained using non-uniform boundary conditions, other mechanical parameters used in FEA simulations are listed in Table 1.

Figure 9 illustrates the theoretical elastographic SNR (SNR$_e$) plot obtained using the specifications of the simulated transducer and the aforementioned signal processing parameters. The theoretical framework proposed by Varghese and Ophir (Varghese and Ophir 1997) was used for generating the theoretical SNR$_e$ curve plot. It is important to note that the theoretical SNR$_e$ curve: 1) assumes one dimensional speckle motion, and 2) joint stationarity of pre- and post-compression signals, 3) neglects frequency dependent attenuation and 4) assumes that the observation window is at the focus of the transducer. In view of these assumptions, the theoretical SNR$_e$ can never be achieved in practice. Nevertheless, the theoretical SNR$_e$ plot can be used as a "gold standard" to evaluate the performance of any strain estimation algorithm. Figure 10 illustrates the signal-to-noise curves estimated using the proposed algorithm and the above listed tracking approaches. Equation (1) was used to estimate the elastographic signal-to-noise ratio (SNR$_e$) from the reconstructed elastograms (O'Donnell, Skovoroda et al. 1994),

$$SNR_e = \frac{s}{\sigma_s} \qquad (1)$$

where s is the average strain estimated over the entire image. σ_s is the variance of strain estimates. The SNR$_e$ curve estimated using the proposed algorithm envelopes the SNR$_e$ curves obtained using the global stretching-based RF data tracking algorithm and the algorithm by Srinivasan et al. (Srinivasan, Kallel et al. 2002). For all values of applied strain, the SNR$_e$ plot obtained from the proposed algorithm was statistically different ($p < 0.05$) from the one obtained using the algorithm proposed by Srinivasan et al. (Srinivasan, Kallel et al. 2002). Analysis of variance was used as a statistical measure for quantifying the differences between the two SNR$_e$ curves. Thirty independent realizations were used for the statistical study. Figure 11 illustrates the image variance estimated at different values of applied strain. As predicted using strain filter theory (Varghese and Ophir 1997), the variances in strain estimation increase non-linearly with applied strain. The rate of increase in variance is lowest when using the proposed algorithm. Figure 12 illustrates the average cross-correlation coefficient (ρ) over the image obtained using different tracking algorithms. The cross-correlation coefficient obtained by tracking the pre- and the post-compression signal can be expressed analytically as:

$$\rho_{ps} = \frac{\sigma_{ps}}{\sqrt{\sigma^2{}_p \sigma^2{}_s}}, \qquad (2)$$ where

$$\sigma_{ps} = \int_{-T/2}^{T/2} S_p(t) S_s(t+\tau) dt, \qquad (3)$$

$$(4)$$

$$\sigma^2{}_p = \int\limits_{-T/2}^{T/2} S^2{}_p(t)dt \tag{5}$$
, and
$$\sigma^2{}_s = \int\limits_{-T/2}^{T/2} S^2{}_s(t)dt.$$

Subscript p denotes pre-compression and s denotes post-compression. T is the tracking window ($W = T{*}c/2$); c is the speed of sound through the tissue. ρ_{ps} is the cross-correlation coefficient. The error bars in Figure 12 illustrate the variance in the average image cross-correlation coefficient obtained from thirty independent realizations. The rate of decrease in the correlation coefficient as a function of applied strain is smallest for the proposed algorithm. Figure 13 illustrates different contrast-to-noise ratio curves- CNR_e (Bilgen and Insana 1997) obtained from the elastograms simulated using different strain estimation algorithms. Contrast-to-noise ratio is expressed as,

$$CNR_e = \frac{abs(s_t - s_b)}{\sqrt{\dfrac{\sigma^2{}_t + \sigma_b{}^2}{2}}} \tag{6}$$

where, s_t is the average strain in the target, and s_b is the average strain of the background. $\sigma^2{}_t$ is the variance of the strain estimates in the target, and $\sigma^2{}_b$ is the variance of the strain estimates in the background. CNR_e values for a range of applied strain (0.5-10%) obtained using the proposed algorithm are 3 dB above the CNR_e curve obtained using the algorithm proposed by Srinivasan et al. (Srinivasan, Kallel et al. 2002) and are 6 dB higher than the RF data tracking algorithm with uniform global stretching (Cespedes and Ophir 1993).
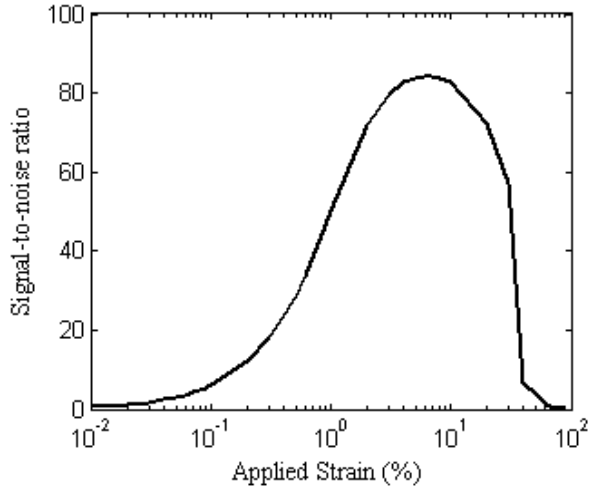

Figure 9: Theoretical SNR$_e$ plot for a range of applied strains. The plot was obtained at 12 MHz center frequency, 40 % fractional bandwidth (-6 dB), system SNR of 30 dB, window length of 2 mm and overlap of 90 %.
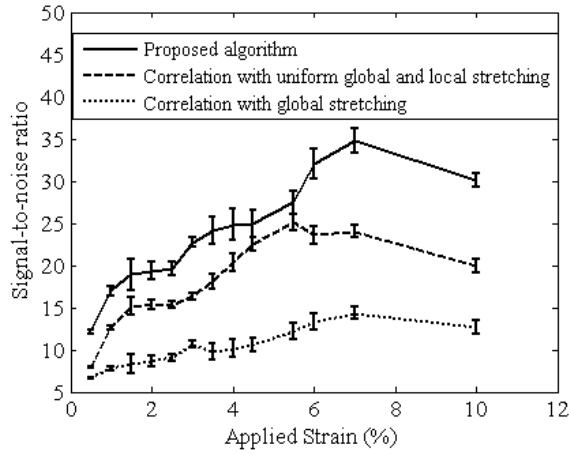
Figure 10: SNRₑ plots comparing proposed algorithm with uniform global stretching only (Céspedes and Ophir 1993), and global followed by local stretching approaches (Srinivasan et al. 2002b).
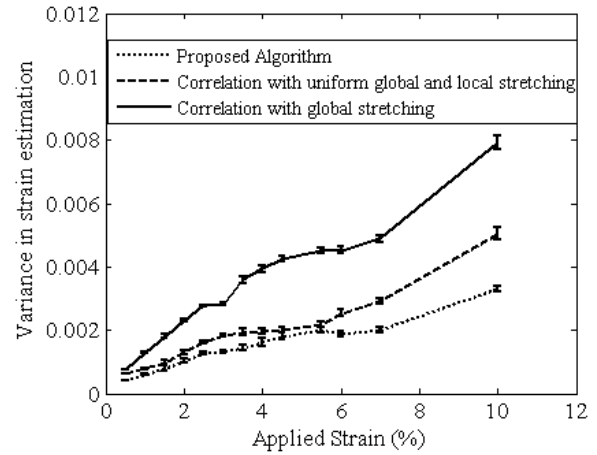

Figure 11: Estimated image variance comparing proposed algorithm with uniform global stretching only (Céspedes and Ophir 1993), and global followed by local stretching approaches (Srinivasan et al. 2002b).
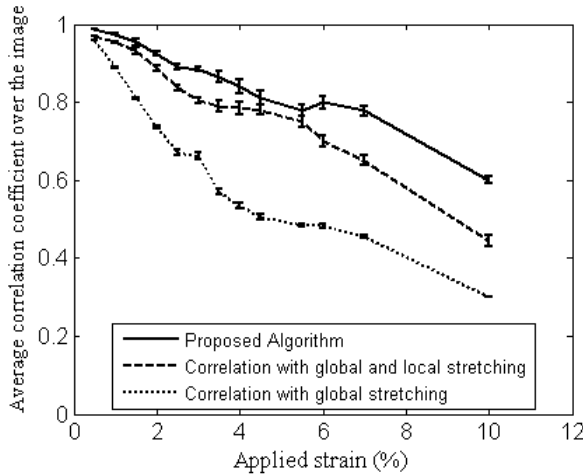

Figure 12: Average cross-correlation coefficient over the reconstructed image obtained using proposed algorithm, algorithm with uniform global stretching only (Céspedes and Ophir 1993), and global followed by local stretching approaches (Srinivasan et al. 2002b).

Figure 13: CNRₑ ratio plots obtained using proposed algorithm, algorithm with uniform global stretching only (Céspedes and Ophir 1993), and global followed by local stretching approaches (Srinivasan et al. 2002b).
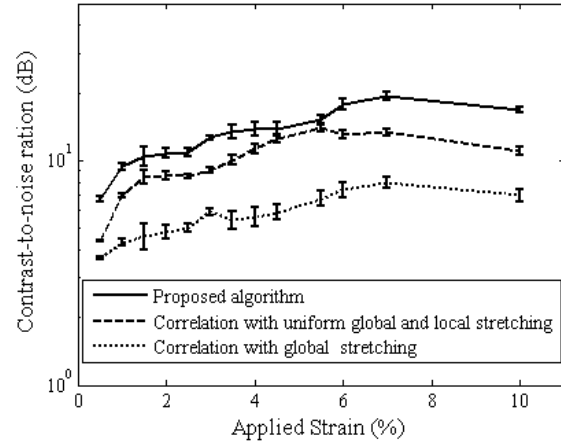
B. Experiments

Experimental evaluation of the tracking algorithm was performed on an acryl-amide based prostate phantom previously fabricated by (Li and Hossack 2005). The mean cross-sectional diameter of the embedded oblong inclusion in the longitudinal (range) direction was approximately 7 mm. A Siemens Sequoia 512 scanner (Siemens Medical Solutions, Mountain View, CA) was used in this study. Multiple demodulated "I/Q" (In-phase/Quadrature) radio frequency beamformed lines of acoustic data were acquired from the ultrasound scanner using a research interface employing an I/Q data capture board. A 192 element, 12 MHz, -6 dB 40 % fractional-bandwidth transrectal ultrasound transducer was used for scanning the prostate phantom. The depth of acquisition was 24 mm and the width of acquisition was 40 mm. The experimental apparatus and the protocols used for the validation are described in (Li et al. 2005) and will be reiterated in detail in the phantom experiment section (Section 6). Fifty frames were acquired such that the total applied strain over 50 frames was 2 %. Every 25th frame (1 and 25-$E_{1, 25}$, 2 and 26-$E_{2, 26}$ and so on...) was tracked. Final elastogram was generated by averaging over five independently obtained elastograms (($E_{1, 25}$ +.....+ $E_{5, 29}$)/5) Figure 14a illustrates an elastogram obtained using the method proposed in this paper. Figure 14b illustrates an elastogram reconstructed by using the algorithm proposed by Srinivasan et al. (Srinivasan, Kallel et al. 2002). As illustrated in Figures 14a and 14b, elastograms generated by the algorithm proposed in this paper provide higher CNR_e and retain the shape of the enclosed inclusion. The depth dependent strain attenuation is clearly visible in the elastograms in Figures 14a and 14b. Thus uniform global stretching over the entire image as suggested in the first stage of the algorithm by Srinivasan results in stretching inaccuracies and is a likely cause of the noise observed in Figure 14b. The algorithm proposed in this paper stretches every A-line by the local strain profile over that A-line as predicted by the B-mode tracking stage (the first stage of the proposed algorithm). Also, the stretching takes into account the strain decay with depth and hence minimizes noise due to stretching inaccuracies, which are likely to occur due to tissue inhomogeneity. The algorithm by Srinivasan et al. requires an *a priori* estimate of the applied strain for stretching the post-compression data, whereas the algorithm proposed in this paper does not have such a requirement. Thus, for trans-rectal, and handheld elastography, the proposed algorithm is expected to exhibit superior performance to algorithm proposed by Srinivasan et al. For the case with uniform boundary condition (as in motion stage based elastography, where the applied strain is known *a priori*), we expect that both algorithms should demonstrate similar performance.
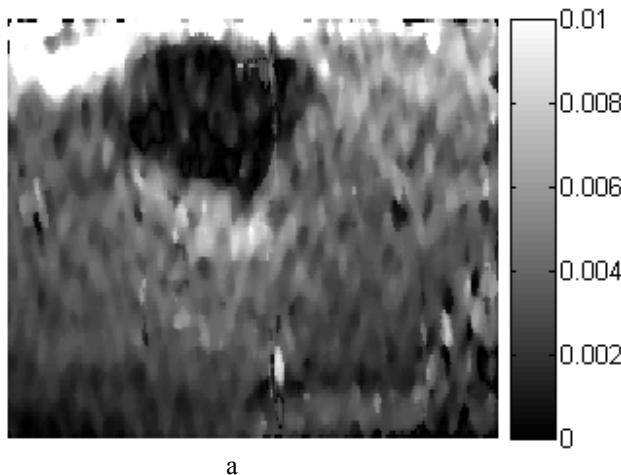

a

b

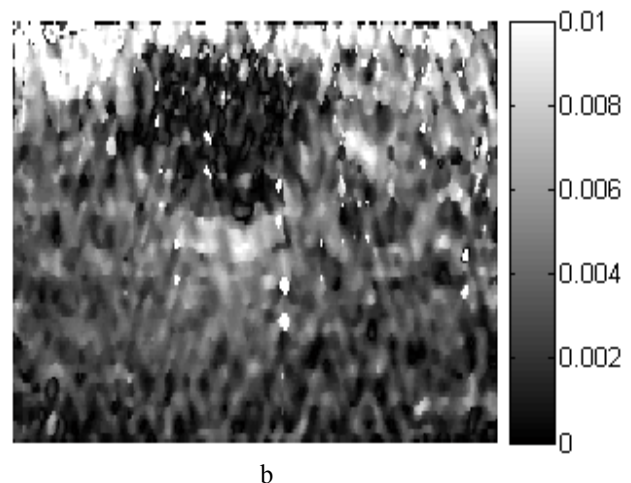**Figure 14a The modulus contrast ratio of the inclusion in the image with respect to the**

Figure 14b: The modulus contrast ratio of

background was 10. A window length of 2 mm and an overlap of 90 % were used for processing the elastogram. The obtained elastogram is an average strain image over 5 frames. The elastogram was reconstructed using the proposed algorithm.

the inclusion in the image with respect to the background was 10. A window length of 2 mm and an overlap of 90 % were used for processing the elastogram. The obtained elastogram is an average strain image over 5 frames. The elastogram was by reconstructed using the algorithm proposed by Srinivasan et al. (2002b).

1.   Rendering 3D shapes of embedded inclusions :Simulations

3D elastographic simulations framework described in section 3 was used for 3D shape rendering study. Two different cases were considered for the 3D rendering study- the axial and the lateral resolution study (Figure 15). The transducer array (Field II) was swept across (along elevation) the inclusions to generate elastograms by 3D rendering. The spiculated inclusion models a malignant lesion, whereas the smooth spherical inclusion models a benign lesion (Ueno 1986, Lee 1988). In the model shown in Figure 15, the background was simulated as a 40x40x40 mm cube with uniform density and stiffness of 4 KPa The inclusion was three times as stiff as the surrounding background. The spherical inclusion had a cross-sectional diameter of 5 mm; whereas the spiculated malignant inclusion had a mean cross-sectional diameter of approximately 6 mm. External displacement was applied to the top surface of the cube as illustrated in Figure 15. Parameters listed in Table 1 were used to for simulations described in this section. The simulated transducer was slowly swept across the top surface of the cube and twenty three pre- and post-compression RF data slices were collected along the elevational dimension. The acquired pre- and post-compression RF data sets were tracked using the algorithm detailed in section 2. Various elastograms obtained along the elevational direction were segmented using 3D gradient vector flow active surface (GVF-AS) algorithm (Tay, Acton et al. 2006) and rendered in 3D to reconstruct the 3D shapes of the inclusions. The strain images obtained directly from the FEA simulations were also segmented and rendered to produce ideal 3D shapes of the modeled inclusions. Figure 16 illustrates the 3D reconstruction from the axial resolution study. The modeled malignant and benign lesions were embedded in the 3D cube and were placed longitudinally along the axis of symmetry. The axial separation between the two lesions was reduced in incremental steps of 0.1 mm. For every step, the lesions were reconstructed from the elastograms and rendered in 3D. The process was repeated until the lesions were close enough to each other such that their reconstruction resulted in one fused entity instead of two distinct entities. The axial resolution of the 3D reconstruction was approximately 0.8 mm (five wavelengths). Figure 16-a illustrates a 3D reconstruction from the generated elastograms, whereas Figure 16-b illustrates a 3D reconstruction from the ideal numerical strain images obtained from the FEA simulations. As expected, the 3D reconstruction from ideal images is sharper than that from the elastogram. Also, the lesions reconstructed from the elastogram exhibit shape warping that can be attributed to limitations arising from the signal processing parameters (window length and window overlap etc.), and the non-uniformity of the sampling of the ultrasound data in the three dimensions. Lateral resolution of the 3D reconstruction was estimated by repeating the steps detailed for the axial resolution study. The lateral resolution of the 3D reconstruction was approximately 1.5 mm (ten wavelengths). Figures 17 a-b illustrate a 3D reconstruction from the lateral resolution study
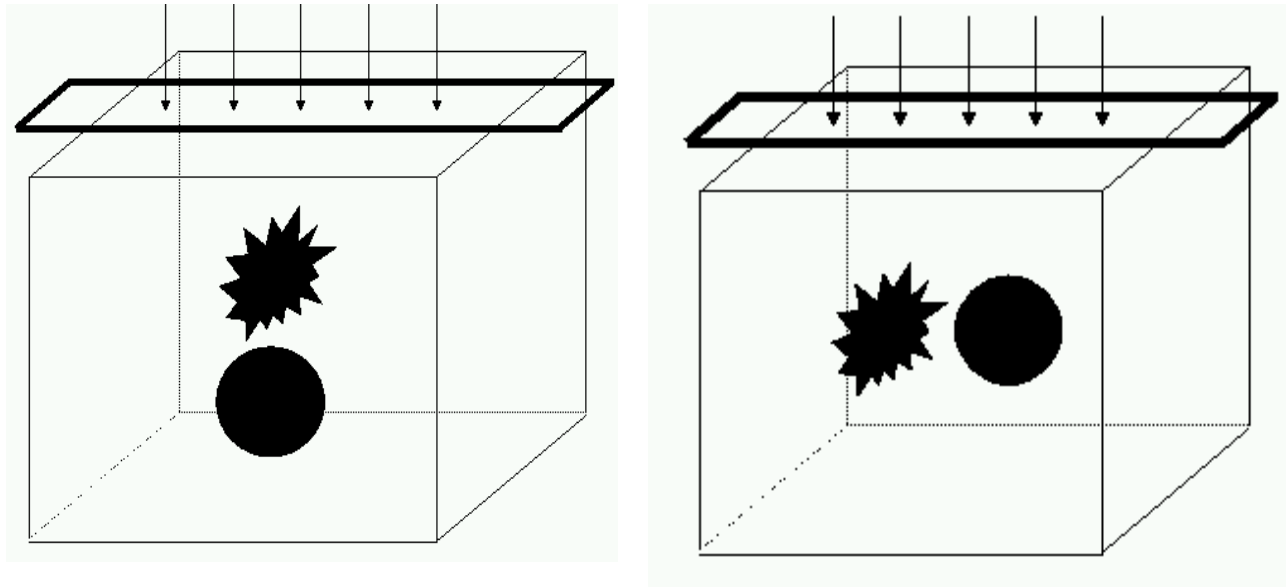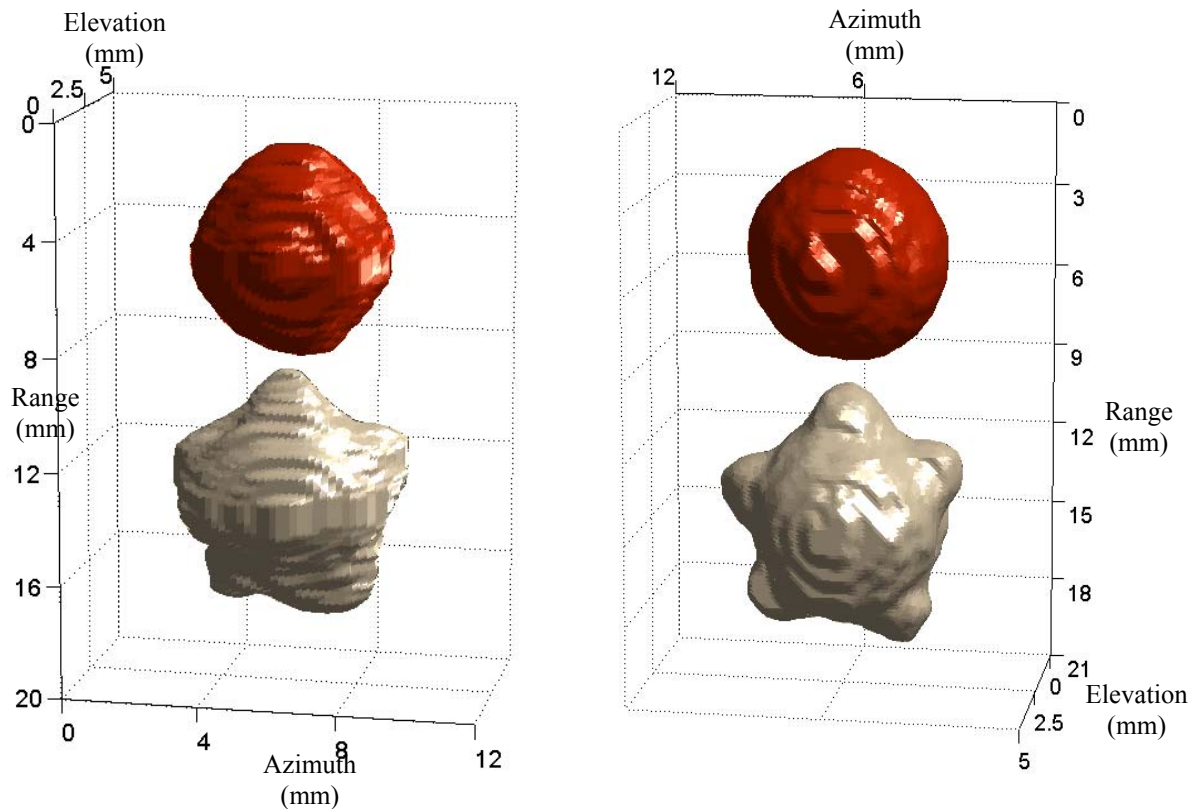
Figure 15: The ᵃ ve figures illustrate the two different simula ᵇ cases considered for the 3D rendering study. The arbitrary shaped inclusion models a malignant lesion, whereas the smooth spherical inclusion models a benign lesion. The cases a and b were considered to evaluate the axial and the lateral resolution of the 3D reconstruction.

.

a)   b)

Figure 16: Axial resolution simulation study: (a) 3D reconstruction from the reconstructed elastograms, (b) 3D reconstruction from the numerical strain images derived from the FEA simulations
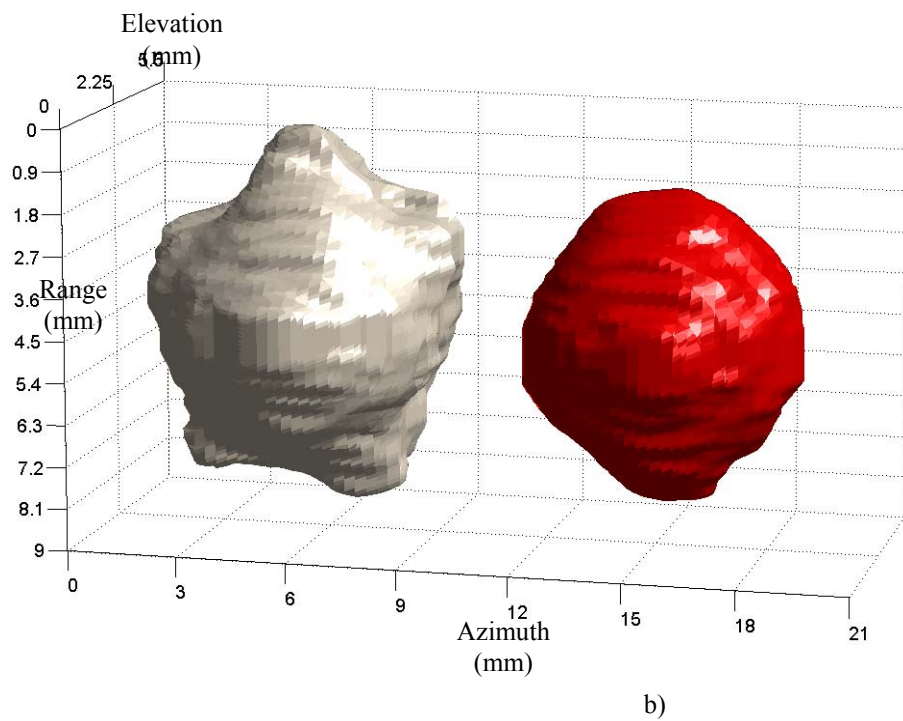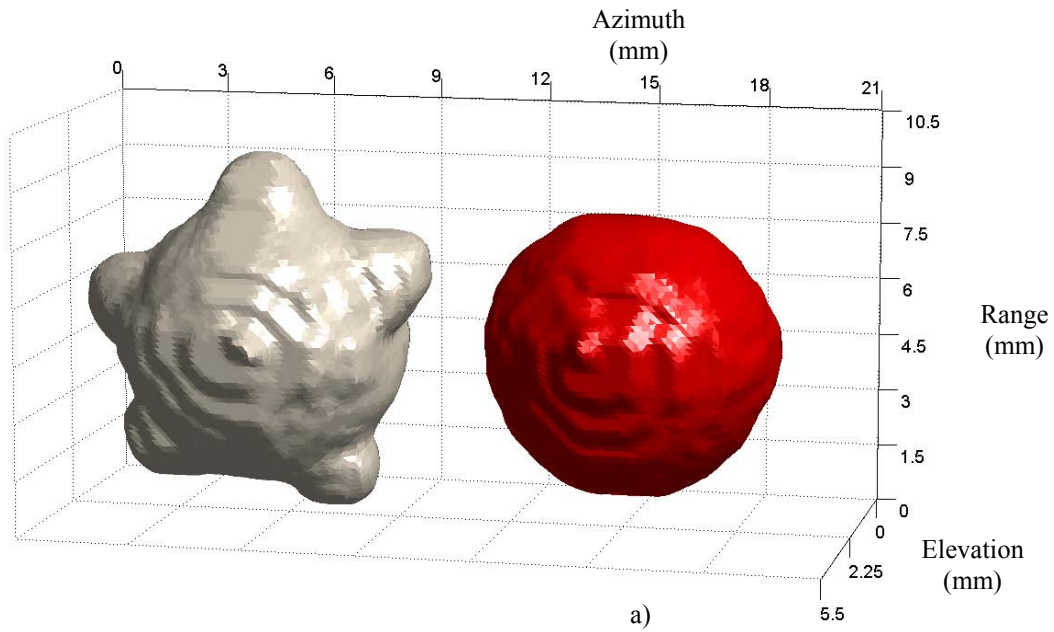
a)

b)

Figure 17: Lateral resolution simulation study: (a) 3D reconstruction from the reconstructed elastograms, (b) 3D reconstruction from numerical strain images derived from the FEA simulations.

2. Elastographic phantom experiments for 3D rendering study

A. A purpose built prostate phantom

The acrylamide-based prostate phantom was fabricated using the protocol published by Negron et al. (Negron, Viola et al. 2002). The prostate phantom consisted of three compartments - the prostate tissue with embedded inclusion, the anal passage, and the surrounding viscera. A schematic of the constructed phantom is illustrated in Figure 18, whereas Figure 19 illustrates a photographic view of the prostate phantom.
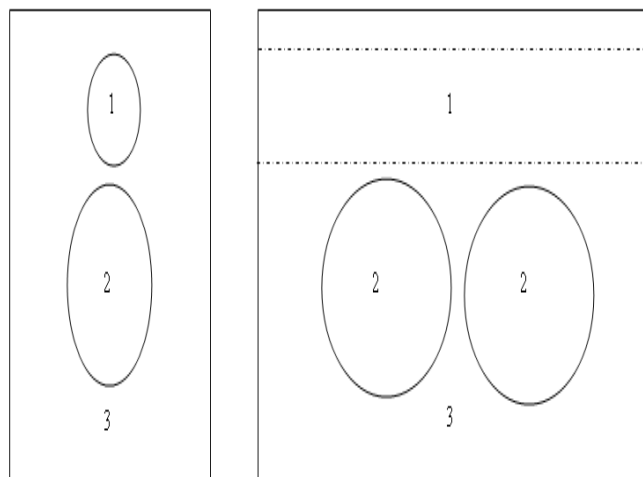

Figure 18: Schematic representation of the prostate phantom. 1: Anal passage, 2: Prostate tissue, 3:Viscera

Figure 19: Prostate phantom- a photographic view.

The prostate material and the surrounding gel (viscera) were composed of a 4% acrylamide solution, while inclusions in the prostates were composed of 8% acrylamide, which imparted different stiffness to the lesion and the surrounding prostate tissue. The Young's modulus for 4 % gel is approximately 4 KPa, whereas it is 16 KPa (Konofagou et al. 2003) in the 8% gel stiff inclusions. Thus, the modulus ratio for all embedded lesions was approximately four. Sephadex (GE-Amersham, Piscatway, NJ) was added to the prostates and inclusions to give speckle; a higher concentration of sephadex was added to the inclusions than the surrounding prostates, yielding a different speckle pattern. Two prostates of approximately 100 mL each were included in the phantom, one containing a spherical inclusions and the other containing an irregular inclusions. The smooth inclusion was approximately 8 mm in diameter whereas the irregular shaped inclusion had a mean diameter of 1 cm. To ensure uniform speckle-pattern in inclusions and prostate, the mixture of different component solutions was enclosed in a latex balloon and was rolled gently for a setting period (approximately 20 minutes following the mixing of components) until the solution had gelled. The rolling protocol mitigates against the settling of the embedded inclusion and may sometimes lead to a situation where two inclusions are placed apposing each other, hence two different prostates were constructed, each embedding one inclusion.

B. " I-Beam" transducer and elastographic phantom experiments

A Siemens Sequoia 512 scanner was used for image acquisition. The prostate phantom was scanned using an "I-Beam" type transducer - a modified linear transducer array consisting of a

central "imaging" array bordered by two perpendicular "tracking" arrays in a cylindrical housing, as illustrated in Figures 20 a-b. Using this configuration, the angular separation between two successive image slices could be tracked by measuring the azimuthal motion in the tracking arrays. The arrays were operated at 12 MHz, using a -6 dB fractional bandwidth of approximately 40 %. A small tube for water delivery was attached to the transducer housing, and the assembly was surrounded with a water-tight latex transducer cover. When acquiring different image slices, the transducer had to be swept at an angle across the region of interest (ROI). This assembly was mounted so that during the angular rotation, translational motion was restricted, facilitating pure rotational motion of the transducer. The mounted transducer was inserted into the prostate phantom and used to perform a series of two-dimensional elastographic scans. At every angular position, the phantom was compressed by injecting water in the transducer sheath via the connected tube using a syringe pump while simultaneously collecting fifty I/Q data frames. For each lesion, gain, field of view, and focal depth were optimized for maximum visibility of that particular lesion. The data were processed offline as detailed in section 2 to generate elastographic image slices.
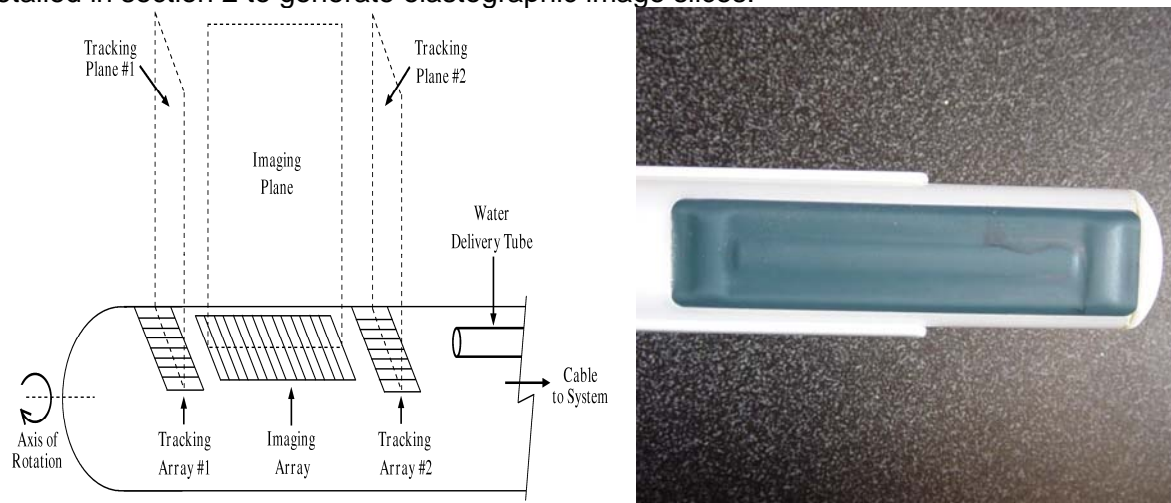

Figure 20: a) Configuration of the modified transducer comprising a central imaging array bordered by two perpendicular tracking arrays. During a scan, the transducer is rotated about its central axis, as indicated, b) A photographic view of prostate probe with tracking and imaging arrays.

C. Experimental results

Elastographic experiments were conducted as described in sub-section B. Both irregular shaped and smooth inclusions were imaged. Sixteen elastographic and sonographic image slices were acquired by sweeping the trans-rectal prostate transducer across the spatial extent of both inclusions. Figure 21 illustrates elastograms and corresponding sonograms for a few angular positions of the trans-rectal prostate transducer while sweeping across the irregular shaped inclusion. Figure 22 illustrates similar images for the smooth shaped inclusion. Figure 23 illustrates images of the smooth lesion reconstructed from sonograms and elastograms, respectively. The shape and the size of the smooth inclusion reconstructed from the sonograms and elastograms are approximately similar; the smooth inclusion reconstructed from elastograms tapers at the longitudinal edges, and is probably due to the low

Figure 21: Few slices across the embedded inclusion mimicking a malignant lesion. Top row illustrates elastograms, bottom row illustrates sonograms. The field of view is 30 x 30 mm.
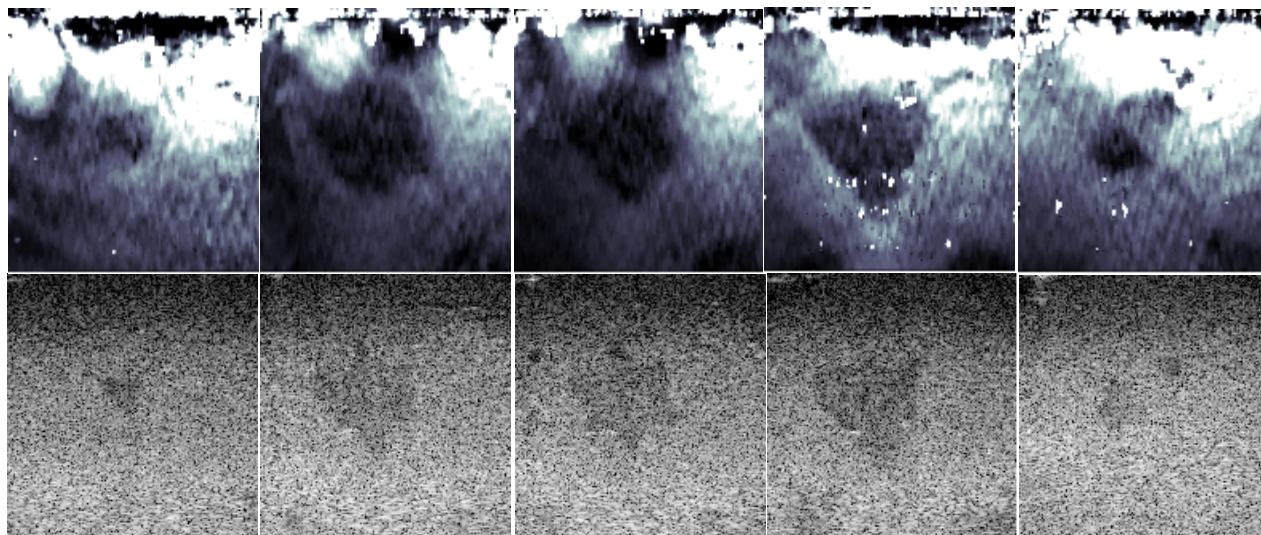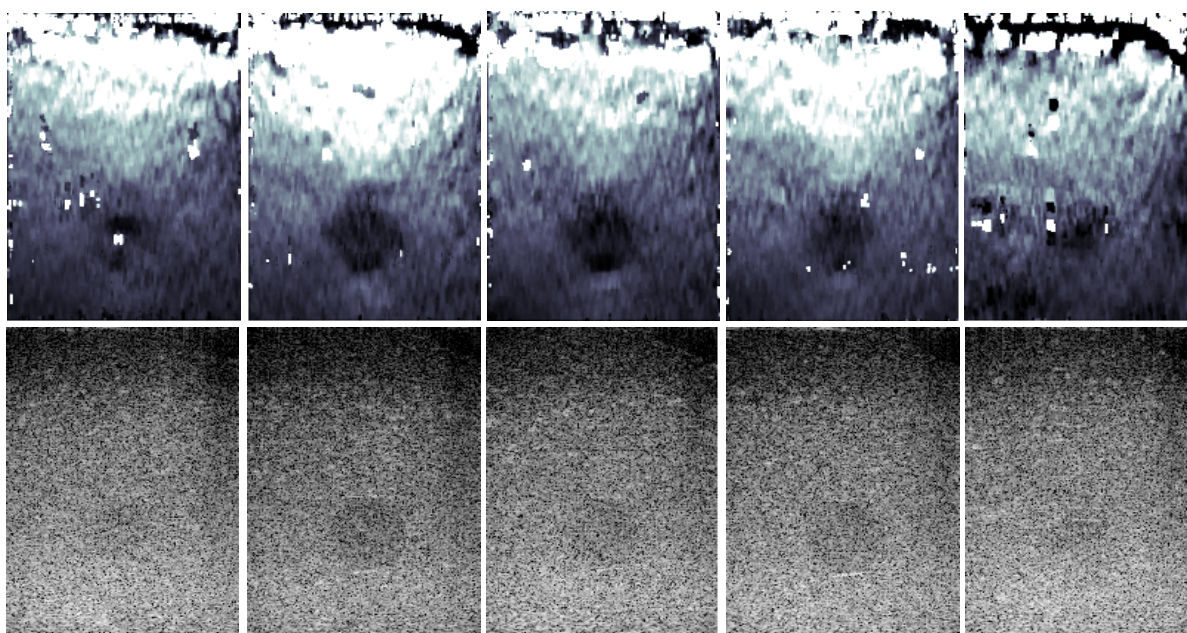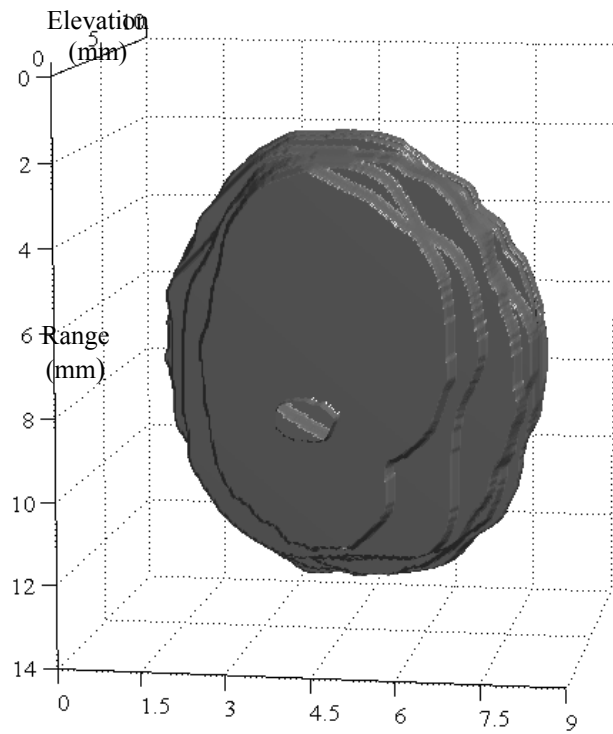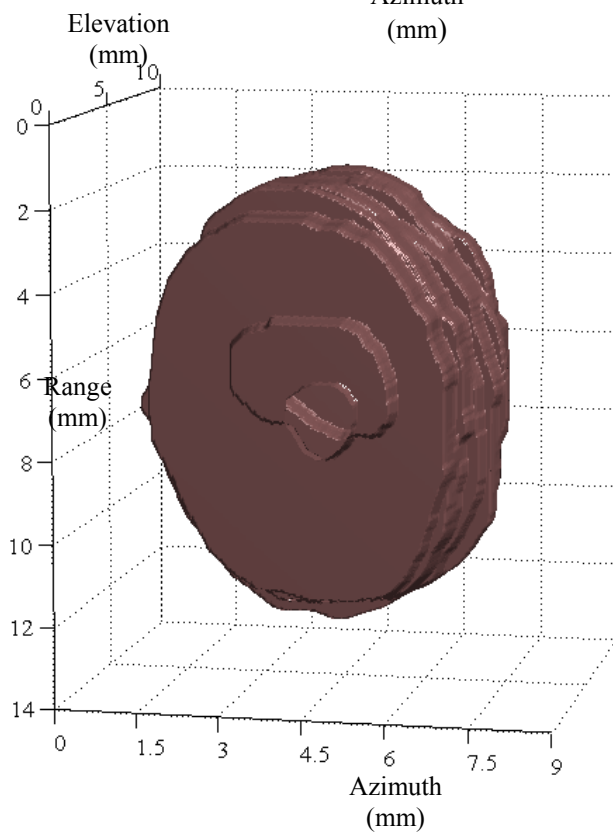

Figure 22: Few slices across the embedded inclusion mimicking a benign lesion. Top row illustrates sonograms, bottom row illustrates elastograms. The field of view is 40 x 30 mm.

Figure 23: a) Smooth inclusion mimicking a benign lesion reconstructed from elastograms. b) Smooth inclusion reconstructed from sonograms.

pass filtering or smoothing effect of the processing windows used for generating elastograms. Figure 24 illustrates the irregular shaped lesion reconstructed from the elastograms and sonograms, respectively. The shape of the irregular shaped inclusion, when reconstructed from the elastograms, has blunt edges and appears larger in size than that reconstructed from the sonogram or B-mode image. Similar results have been reported by Garra et al. (Garra, Céspedes et al. 1997) where the authors demonstrate the same by comparing the sonographic and elastographic images for an irregular shaped malignant cancer in in-vivo human scans. Thus, we contend that the 3D size and the shape of the reconstructed lesion (inclusion) have the potential to assist in discriminating benign cancers from malignant cancers.

Figure 24: a) Irregular shaped inclusion mimicking a malignant lesion reconstructed from elastograms. b) Irregular shaped lesion inclusion reconstructed from sonograms.

Discussion

In elastography, image quality is contingent upon accurate estimation of internal tissue displacements. Signal companding is a simple, yet elegant, approach of improving elastographic image quality. In the second section of this article, we proposed an adaptive stretching based tracking algorithm. The algorithm takes into account the local variations in tissue elasticity and performs iterative local stretching, which provides a superior CNR_e to previously proposed adaptive tracking algorithms (Srinivasan, Kallel et al. 2002). When encountering non-uniform boundary conditions, as in prostate elastography, the proposed algorithm is expected to perform better than conventional stretching based algorithms as they require an *a priori* estimate of the applied strain. When using an ultrasound scanner operating at higher frame rates with a high bandwidth transducer and performing handheld or trans-rectal prostate elastography, the net motion between the consecutive image frames may be small. Thus, the correlation-based tracking in the first two stages of this algorithm may be replaced by a sum-of-absolute-difference approach (Chaturvedi, Insana et al. 1998), whereas the third stage may be replaced by temporal tracking of zero crossings of the pre- and post-compression echo RF signals. Thus, a reduction in computation time may be achieved by an order of magnitude without any substantial degradation in image quality. Such a modified algorithm, when implemented on FPGA's, can be easily incorporated into programmable scanners such as the ULTRASONIX RP (Richmond, BC) and may help in real time tissue elasticity imaging. In a PC based environment, real-time image registration and rendering algorithms may be used to render multiple image slices to accurately reconstruct a 3D volumetric elastogram. For this work, the elevational resolution is expected to be a function of the greater of the two properties of the data set, the elevational beam width and the angular separation between two consecutive slices and intuitively may be assumed to be a linear function of depth as the separation between two consecutive slices increases linearly as a function of depth. Thus, for detecting and rendering smaller lesions deep in tissue, it may be essential to have sufficiently high angular sampling in addition to having a higher image frame rate. Nevertheless, such 3D elastography imaging systems may be used for a variety of applications such as real-time volumetric monitoring of HIFU lesions, real-time volumetric estimation of viscous properties of tissue using non-linear or sinusoidal compression techniques between consecutive image frames thereby imaging the temporal behavior of the tissue strain, and temporal monitoring of the growth of cancers.

Publications arising from research (attached to this document)

3D prostate elastography: algorithm, simulations and experiments
A V Patil, C D Garson and J A Hossack,
Physics in Medicine and Biology (52) pp3643–3663, 2007

Our prostate cancer diagnosis method is dependent on our ability to resolve regions of the prostate with anomalous elasticity. Ultimately, our ability to resolve fine anomalous features depends on data quality (signal to noise ratio, imaging resolution, etc.) and the performance of the displacement tracking algorithm. In this paper, a new multi-resolution hybrid strain estimator is discussed. The estimator is initialized using the B-mode tracking stage for the sake of speed of operation. Nonlinear and linear stretching are applied in successive radio frequency (RF) tracking stages for refining the estimated axial and lateral displacements. A staggering operator was used to obtain strain images from the reconstructed axial displacements. Simulations and experiments, using a 12 MHz frequency, 40% -6dB fractional bandwidth, 128 element transducer (0.2 mm pitch), a elastographic window length of 2mm and 90% window overlap, produced a 3–6 dB improvement in the elastographic contrast-to-noise ratio over the results obtained using conventional multi-stage stretching based strain estimators. The average image cross-correlation coefficient obtained using the proposed algorithm was improved by 6–8%. 3D elastographic simulations conducted to study the performance of a 3D elastographic imaging framework predict achievable axial and lateral resolutions of approximately five and ten wavelengths, respectively. A close correspondence between inclusions reconstructed from experimental elastograms and the known physical shape of actual 3D inclusions shows the potential application of 3D elastography for identifying and classifying the detected lesions (invisible in sonograms) on the basis of their shape.

3D Segmentation of the prostate via poisson inverse gradient initialization
B. Li, A.V. Patil, J.A. Hossack and S.T. Acton
Proc. IEEE Int. Conf. on Image Processing, 2007 (conference paper)
Automatic active model initialization via Poisson inverse gradient
B. Li and S.T. Acton
IEEE Transactions on Image Processing, Vol. 17, No. 8 pp1406-1420 2008 (journal paper)

Accurate segmentation and volumetric assessment of the prostate is critical to assessment of cancer progression. 3D segmentation is also important in treatment involving both radiotherapy and brachytherapy. A new 3D segmentation solution for ultrasound images of the prostate based on deformable surfaces is discussed in this paper. The deformable surfaces were driven by the vector field convolution (VFC) external force model. This external force has high computational efficiency and excellent solution quality in comparison with many existing techniques such as gradient vector flow (GVF). A key aspect of the segmentation solution proposed here is the ability to automatically initialize the deformable surface in 3D. The initialization method exploits a Poisson inverse gradient (PIG) technique that solves the inverse problem from the external force field to the external energy and determines the highest probability coarse segmentation. We validated the 3D segmentation on simulated images of the prostate. Furthermore, simulated data showed that Poisson Inverse Gradient (PIG) initialization resulted in a 60% reduction in segmentation error for high curvature

contours. Examples and comparisons with two state-of-the art automatic initialization methods were presented to illustrate the advantages of this innovation, including the ability to choose the number of active models deployed, rapid convergence, accommodation of broken edges, superior noise robustness, and segmentation accuracy.

KEY RESEARCH ACCOMPLISHMENTS

- Completed Aims 1, 2 and 3. We designed and had fabricated a very high resolution transrectal ultrasound transducer array for high resolution prostate imaging.
- Integrated the new transducer with an ultrasound scanner and an automated injection stage to realize an accurate elastographic imaging device.
- Tested the 3D and elastographic imaging capability of the transducer / scanner.
- Developed new ultrasound speckle reduction techniques suitable for prostate ultrasound.
- Developed new algorithms – fine tuned for 3D prostate ultrasound images - for segmenting selected tissue regions (i.e. the prostate outline and / or suspected cancer) in an automated manner. (Li, Patil et al. 2007; Li and Acton 2008)
- Developed new ultrasound signal tracking techniques that improve the quality of ultrasound derived 3D measures of elastic anomaly as might be very useful in the more sensitive and more specific detection of prostate cancer.(Patil and Hossack 2007)

REPORTABLE OUTCOMES

(The first three of these, our most recent results, are in included the appendix)
B. Li, A.V. Patil, J.A. Hossack and S.T. Acton, "3D Segmentation of the prostate via poisson inverse gradient initialization," Proc. IEEE Int. Conf. on Image Processing, San Antonio, Texas, September 16-19, 2007.
A.V. Patil, J.A. Hossack "3D prostate elastography: algorithm, simulations and Experiments" Physics in Medicine and Biology (52) pp3643–3663, 2007
B. Li and S.T. Acton, "Automatic active model initialization via Poisson inverse gradient," IEEE Transactions on Image Processing, Vol. 17, No. 8 pp1406-1420 2008.

Y. Li, A. Patil and J. A. Hossack, "High resolution three-dimensional prostate ultrasound imaging". Presented at SPIE Medical Imaging, San Diego, CA, 2006
Y. Li, A. Patil and J. A. Hossack, "Combined elasticity and 3D imaging of the prostate" Proceedings of 2005 IEEE Ultrasonics Symposium, pp.1435-1438, 2005
P. C. Tay, S. T. Acton and J. A. Hossack, "A Stochastic Approach to Ultrasound Despeckling", Accepted for presentation at 2006 IEEE International Symposium for Biomedical Imaging: From Nana to Macro Arlington, VA, 2006

CONCLUSIONS

Our approach combines using an "I-Beam" transducer with 3D capability and elasticity imaging. We tested our prototype transducer and system using a prostate tissue-mimicking phantom. The prostate strain imaging performed here using a slightly inflated sheath over the transrectal transducer significantly enhanced tumor visibility (a hard inclusion in the phantom). The lesion was practically invisible in the regular B-mode image.

The I-Beam transducer enabled reconstruction of discrete 2D image acquisitions into 3D regular spaced orthogonal grid space, and thereafter the tumor was rendered in 3D. The volume calculated for this tumor had an error of approximately 11% compared to the independently determined volume.

Additionally, we have made significant progress in the area of image speckle reduction pre-processing and in image feature segmentation. These image processing contributions significantly enhance the practical utility of our technique since they hold the promise of

accelerating the prostate cancer diagnostic task and reducing intra and inter operator variability. Reducing variability is significant since serial analysis of cancer growth or remission is dependent on accurate and repeatable measures of prostate volume. Since we are able to measure volumes directly, rather than extrapolating volume from a length dimension or cross-sectional area, our image contributions are well-matched and complement our contributions in 3D and elastographic imaging.

Significance in plain English:

Our improved prostate ultrasound imaging techniques have the potential to detect prostate cancer earlier and with more reliability (i.e. improved sensitivity and specificity). In this way, we believe that our research has a useful public health contribution.

Personnel supported under this grant:

PI: John A. Hossack, Ph.D.
Co-I Scott T. Acton, Ph.D.
Co-I Dan Theodorescu, M.D., Ph.D.
Co-I Laurence R. Watson, R.D.M.S.
Graduate Research Assistant: Abhay V. Patil, M.S.
Graduate Research Assistant: Christopher D. Garson, B.S.
Graduate Research Assistant: Yinbo Li, Ph.D.

REFERENCES:

Alam, S., E. Fellepa, et al. (2004). "In vivo Prostate Elastography: Preliminary Results." <u>Proceedings of IEEE Ultrasonics Symposium</u>.

AmericanCancerSociety (2008). "American Cancer Society Prostate Cancer Statistics from <u>www.cancer.org.</u>"

Bilgen, M. and M. Insana (1997). "Predicting target detectability in acoustic elastography." <u>Proc. IEEE Ultrason. Symp</u> 2: 1427-1430.

Cespedes, I. and J. Ophir (1993). "Reduction of image noise in elastography." <u>Ultrason Imaging</u> 15: 89–102.

Chaturvedi, P., M. Insana, et al. (1998). "Testing the limitations of 2-D companding for strain imaging using phantoms." <u>IEEE Transactions on Ultrasonics Ferroelectrics & Frequency Control</u> 45(4): 1022-1031.

Clements, R. (2002). "The Role of Transrectal Ultrasound in Diagnosing Prostate Cancer." <u>Current Urology Reports</u> 3: 194-200.

Crawford, E., S. Leewansangtong, et al. (1999). "Efficiency of Prostate-Specific Antigen and Digital Rectal Examination in Screening, Using 4.0 ng/mL and Age Specific Reference Range as a Cutoff for Abnormal Values." <u>The Prostate</u> 38: 296-302.

Elman, H. and E. Agron (1989). "Ordering techniques for pre-conditioned conjugate gradient method on parallel
computers." <u>Comput. Phys. Commun</u> 53: 253–269.

Frauscher, F., A. Klauser, et al. (2001). "Detection of Prostate Cancer with a Microbubble Ultrasound Contrast Agent." <u>The Lancet</u> 357: 1849-1850.

Frost, V., J. Stiles, et al. (1982). "A model for radar images and its applicationto adaptive digital filtering of multiplicative noise,." <u>IEEE Trans. Pattern Anal. Machine Intell</u> 4(2): 157-166.

Garra, B. S., I. Céspedes, et al. (1997). "Elastography of Breast lesions: initial clinical results." <u>Radiology</u> 202: 79-86.

Halpern, E., P. McCue, et al. (2002). "Contrast-enhanced US of the Prostate with Sonozoid: Comparison with Whole-Mount Prosatectomy Specimens in 12 Patients." <u>Radiology</u> 222: 361-366.

Hossack, J., T. Sumanaweera, et al. (2000). <u>Quantitative 3D Ultrasound Imaging Using an Automated Image Tracking Technique</u>. IEEE Ultrasonics Symposium, IEEE.

Jensen, J. and N. Svendsen (1992). "Calculation of Pressure Fields from Arbitrarily Shaped, Apodized and Excited Ultrasound Transducers." <u>IEEE Transactions on Ultrasonics Ferroelectrics & Frequency Control</u> 39: 262-267.

Kailath, T. (1976). "Equations of Wiener-Hopf type in filtering theory and related applications." <u>Norbert Wiener: Collected Works vol. III, P. Masani, Ed., Cambridge, MA: MIT Press</u>: 63-94.

Kuan, D., A. Sawchuk, et al. (1985). "Adaptive noise smoothing filter for images with signal-dependent noise." <u>IEEE Trans. Pattern Anal. Machine Intell</u> 7(2): 165-177.

Lee, J. (1980). "Digital image enhancement and noise filtering by use of local statistics." <u>IEEE Trans. Pattern Anal. Machine Intell</u> 2(2): 165-168.

Li, B. and S. Acton (2008). "Automatic active model initialization via Poisson inverse gradient." <u>IEEE Transactions on Image Processing</u> 17(8): 1406-1420

Li, B., A. Patil, et al. (2007). "3D Segmentation of the prostate via poisson inverse gradient initialization." <u>Proc. IEEE Int. Conf. on Image Processing</u>.

Li, Y. and J. Hossack (2005). "Combined elasticity and 3D imaging of the prostate." <u>Proceedings of SPIE Medical Imaging</u> 5750: 7-15.

Lorenz, A., H. Sommerfeld, et al. (1999). "A new system for the acquisition of ultrasonic multicompression strain images of the human prostate in vivo." <u>IEEE Transactions on Ultrasonics Ferroelectrics & Frequency Control</u> 46: 1147-1154.

Loupas, T., W. McDicken, et al. (1989). "An adaptive weighted median filter for speckle suppression in medical ultrasonic images." <u>IEEE Trans. Circuits Syst.</u> 36(1): 129-135.

Lubinski, M., S. Emelianov, et al. (1999). "Speckle tracking methods for ultrasonic elasticity imaging using short-time correlation." <u>IEEE Transactions on Ultrasonics Ferroelectrics & Frequency Control</u> 46(1): 82-96.

Lubinski, M., S. Emelianov, et al. (1996). "Lateral Displacement Estimation using Tissue Incompressibility." <u>IEEE Transactions on Ultrasonics Ferroelectrics & Frequency Control</u> 43: 247-256.

Nagao, M. and T. Matsuyama (1979). "Edge preserving smoothing." <u>Computer Graphics and Image Processing</u> 9(4): 394-407.

Negron, L., F. Viola, et al. (2002). "Development and characterization of a vitreous mimicking material for radiation force imaging." <u>IEEE Transactions Ultrasonics, Ferroelectrics and Frequency Control</u> 49(11): 1543-1551.

Nightingale, K., R. Nightingale, et al. (2000). "A finite element model of remote palpation

of breast lesions using ultrasonic radiation force: factors affecting tissue displacement." <u>Ultrasonic Imaging</u> 22: 35–54.

O'Donnell, M., A. Skovoroda, et al. (1994). "Internal Displacement and Strain Imaging Using Ultrasonic Speckle Tracking." <u>IEEE Transactions on Ultrasonics Ferroelectrics & Frequency Control</u> 41(3): 314-325.

Patil, A. and J. Hossack (2007). "3D prostate elastography: algorithm, simulations and

Experiments." <u>Physics in Medicine and Biology</u> 52: 3643–3663.

Patil, A., T. Krouskop, et al. (2008). "On the effect of 3D tissue motion on ultrasound elastography:

a simulation study - in preparation." <u>Ultrasound in Med. & Biol.</u>

Phillips, P. (2001). "Contrast Pulse Sequences (CPS): Imaging non-linear microbubbles." <u>Proceedings of the 2001 IEEE Ultrasonics Symposium</u> 2: 1739-1745.

Sarvazyan, A. (1998). "Mechanical imaging: a new technology for medical diagnostics." <u>Journal of Medical Informatics</u> 49(2): 195-216.

Srinivasan, S., F. Kallel, et al. (2002). "Analysis of an adaptive strain estimation technique in

elastography." <u>Ultrason Imaging</u> 24: 109–118.

Tay, P. C., S. T. Acton, et al. (2006). "Ultrasound despeckling using an adaptive window stochastic approach." <u>Proc. IEEE Int. Conf. on Image Processing</u>.

Taylor, J., K. Gancarczyk, et al. (2002). "Increasing the number of core samples taken at prostate needle biopsy enhances the detection of clinically significant prostate cancer." <u>Urology</u> 60(5): 841-845.

Toubert, M., M. Schlageter, et al. (1990). "Screening for cancer of the prostate using prostate-specific antigen." <u>Presse Medicale</u> 19(24): 1139-1142.

Varghese, T. and J. Ophir (1997). "A theoretical framework for performance characterization of elastography: the strain

filter." <u>IEEE Transactions on Ultrasonics Ferroelectrics & Frequency Control</u> 44: 164-172.

Walker, W. and G. Trahey (1995). "A fundamental limit on delay estimation using partially correlated speckle signals." <u>IEEE Transactions on Ultrasonics Ferroelectrics & Frequency Control</u> 42: 301-308.

Weiss, R., V. Hartanto, et al. (2001). "In vitro trial of the pilot prototype of the prostate mechanical imaging system." <u>Urology</u> 58(6): 1059-1063.

Xu, C. and J. Prince (1998). "Snakes, Shapes and Gradient Vector Flow." <u>IEEE Trans. Image Processing</u> 7(3): 359-369.

Yu, Y. and S. Acton (2002). "Speckle reducing anisotropic diffusion." <u>IEEE Transactions on Image Processing</u> 11: 1260-1270.